Journal Pre-proofs

Numerical-based Analytical Model of Double-layer Steel-LHDCC Sandwich Composites under Punching Loads

Wei ZHANG, Zhenyu HUANG, Jianqiao YE, Youtam

Numerical-based Analytical Model of Double-layer Steel-LHDCC Sandwich Composites under Punching Loads

Wei ZHANG[1], Zhenyu HUANG[*1,2], Jianqiao YE[3], Youtam[2]

1 Guangdong Provincial Key Laboratory of Durability for Marine Civil Engineering, Shenzhen University, Shenzhen, China 518060.

2 Key Laboratory for Resilient Infrastructures of Coastal Cities (Shenzhen University), Ministry of Education, Shenzhen, China 518060.

3 Department of Engineering, Lancaster University, Lancaster LA1 4YR, UK

Abstract

This study conducts numerical analyses on a newly developed double-layer steel-lightweight high ductility cement composite (LHDCC)-steel sandwich panel under concentrated punching load. Energy absorption ability serves as an important criterion in evaluating the performance of the protective sandwich structures. One critical factor related to energy absorption ability is the stiffness or the deformation capacity of the structure. The present study first develops a procedure to establish a FE model of the double-layer SCS panel. The Concrete Damage Plasticity (CDP) model is adopted to simulate the behavior of LHDCC, with a compressive stress-strain relation represented by a statistically stochastic damage constitutive model. The FE model is validated through comparisons with the test results of 2 single-layer SCS panels and 8 double-layer SCS panels. A series of parametric studies are then performed to check the influences of concrete height, shear span, steel plate thickness, shear connector spacing, loading patch size, concrete strength and steel plate strength on the stiffness and load resistance of the panel. Finally, the paper develops a simplified analytical model to predict the stiffnesses at both elastic and plastic stages, and proposes an idealized load-displacement model to reproduce the load-deformation relation for the double-layer SCS panels. The comparisons with the test and FE results validate the accuracy of the analytical model.

Keywords: *Steel-Concrete-Steel; Lightweight concrete; Stiffness; Double layer; Finite Element*.

* Corresponding author. Email: huangzhenyu@szu.edu.cn

1. Introduction

Compared to conventional Reinforced Concrete (RC) structures, Steel-Concrete-Steel (SCS) sandwich structures show superior advantages, including higher ductility, integrity, load carrying capacity and energy absorption ability [1-5]. The external steel skin plates ensure impermeability of the structure and provide excellent impact and blast resistances [6-10]. In practice, SCS structures are commonly used as protective structures in nuclear engineering, shear walls and bridge decks in construction engineering, as well as marine and offshore structures like storages vessels, ship hulls, oil production platforms, etc. [11-16]. For ships and offshore platforms working in the Arctic region, SCS structures may suffer unevenly distributed ice-contact pressure, with the surface pressure extremely larger than 15 MPa in a localized interaction zone [17-19]. Therefore, the resistances of SCS structures to local punching or local impact require careful considerations in the design.

Extensive investigations have been conducted on load bearing capacity of SCS beams subjected to shear or SCS panels subjected to punching. The experimental data [20-23] on SCS beams reveal that beams with small shear span-to-depth ratio (2.5 to 3.5) always exhibit a transverse shear failure with critical diagonal crack. For partial composite SCS beams, bond-slip appear between concrete and steel plate, which relieves the loading on the steel plate and weakens the ultimate resistance of the structure [24]. Based on Eurocode 2 [25] and ACI 349 [26] for RC beams, bond-slip effect has been considered [27, 28] to predict transverse shear resistance of SCS beams. As regard SCS panels, loads are transferred in three directions and all the materials are under tri-axial stress states. The experimental studies in [29, 30] report that two peak resistances exist on the load-displacement curve, the first of which indicates flexural yielding or punching shear failure of concrete, and the second of which indicates punching shear fracture of steel plate [31]. The resistance due to flexural yielding was addressed according to the yield line theory, while the resistances due to punching shear failure of concrete and punching shear fracture of steel plate were solved by considering concrete, steel plate and shear connectors, independently. Some researchers have also investigated the behavior of curved SCS shells and developed relevant equations to predict their ultimate resistances [32-35].

However, the objective of the past studies focuses on single-layer SCS sandwich composite structures, one drawback of which is that the mechanical compacities of materials are not efficiently and economically utilized due to local failure. To make efficient use of composite materials and improve loading capacity of sandwich composites, Huang et al. [36] developed a double-layer SCS panel using ultra-lightweight and high ductility cement composite as core concrete. The ultimate resistance is significantly increased due to both the material and structural interactions. For a protective SCS panel, another critical factor determining its structural performance is energy absorption ability, which is directly related to deformation capacity. However, to the best knowledge of the authors, existing references on stiffness of single-layer SCS panels are rare to find, so much so that there is no reported work double-layer SCS panels in the literature. In addition, experimental investigations are costly and only provide limited number of test results. As an alternative approach, Finite Element (FE) method solves these problems and is able to simulate nonlinear behavior of SCS panels with various sizes, dimensions, and material properties. More information can be extracted from FE simulation, such as strains and stresses, interactions between concrete, shear connectors and steel plates, damage evolution in concrete during loading process, etc.

The present study aims to investigate the stiffness of double-layer SCS sandwich panels using the FE approach. First, an experimental program on SCS panels subjected to concentrated punching load is briefly introduced. Then, an advanced FE model of double-layer SCS panels is established and validated by test results. After that, a series of parametric analyses is performed by varying concrete height, shear span, steel plate thickness, shear connector spacing, loading patch size, concrete strength, and steel plate strength. Finally, a simplified analytical model is developed to predict the stiffnesses at the elastic stage and plastic stage, respectively, and an idealized load-displacement model is proposed for double-layer SCS panels.

2. Experimental Investigation

Two single-layer and eight double-layer steel-LHDCC-steel sandwich composite panels under concentrated punching load were tested. The LHDCC was designed and made with a compressive cylinder strength of around 45 MPa and a density of around 1450kg/m^3. The ductility of the LHDCC was improved by adding low content polyethylene (PE) fibers (0.7%).

The types of shear connectors include J-hooks, headed studs and hybrid connectors. The material properties of the steel plate, J-hook and headed stud were measured through tensile material tests. Table 1 lists the geometric dimensions and material properties of the panels. Figure 1(a) shows the test set-up and loading scheme of the experimental program. Each specimen was transversely loaded by a square patch at the center of the faceplate, and simply supported on four solid rollers along the edges. The loading was recorded from the Bangwei universal test machine and the displacement at the center of the bottom panel was measured by a Linear Variable Differential Transformer (LVDT).

The experimental program investigated the failure modes and load-displacement responses of each specimen. All the load-displacement curves exhibit two or three peak points indicating different failure modes in the loading history. For the two single-layer sandwich panels, the one with larger shear span-to-depth ratio failed by flexural yielding of the bottom steel plate at the first peak, while the one with smaller shear span-to-depth ratio failed by punching shear failure of concrete at the first peak. Both the two failed by punching shear fracture of the top steel plate at the second peak. For the eight double-layer sandwich panels, all the specimens failed by punching shear failure of concrete at the first peak load. At the second peak load, however, the ones with full composite action failed by punching shear fracture of the top steel plate, while the ones with partial composite action failed by punching shear fracture of the top steel plate accompanied with bond-slip between the concrete and steel plates, as shown in Fig. 1(b)-(c). The load-displacement curve would exhibit a third peak load if the specimen was kept loading until the middle steel plate was punched through. Due to the load resistance of the middle steel plate, the double-layer sandwich panel shows larger load bearing capacity, larger residual strength, better ductility, and energy absorption ability compared to that of the single-layer sandwich panel.

3. Numerical Modelling

The study carried out a series of numerical analyses to investigate load transfer mechanism, failure mode, stiffness, ductility, and energy absorption ability of the double-layer sandwich panels through the advanced commercial software, ABAQUS. First, a systematical procedure is established in this section to model the double-layer sandwich panel subjected to

concentrated patch loading. Then, the finite element model is validated against the experimental results reported in Section 2.

3.1 Material model of concrete

Figures 2(a)-(b) display the compressive and tensile stress-strain curves of the LHDCC obtained from standard material tests of concrete cylinders subjected to axial compression and concrete coupons subjected to axial tension, respectively. The developed LHDCC consists of PII 52.5 R Portland cement (OPC), ultrafine silica fume (SF), granulated ground blast furnace slag (GGBFS), and 0.7% PE fibers. Table 2 lists the mix proportion of the LHDCC, and Table 3 lists the mechanical properties of the surface treated PE fiber. The LHDCC has an elastic modulus of around 14 GPa, a compressive cylinder strength of around 45 MPa, and a tensile strength of around 1.6 MPa. The compressive cube strength of concrete is obtained by multiplying the cylinder strength with the factor of 1.25. Due to the bridging effect provided by the PE fibers, the tensile stress-strain relationship of the LHDCC exhibits an excellent ductile behavior with a long stage of strain hardening, which is around 3%~4% tensile strain and qualified as an Engineering Cement Composite (ECC) material [37, 38]. However, the PE fibers have marginal influences on the compressive behavior of the LHDCC.

The concrete core contributes primarily to the load bearing capacity of the SCS sandwich panel, thus an appropriate representation of the material property of concrete is essential to ensure accuracy of the FE simulation. ABAQUS provides three types of material models for concrete, namely the brittle cracking model, smeared cracking model, and the concrete damage plasticity (CDP) model. Among these three models, the CDP model representing inelastic behavior of concrete as isotropic compressive and tensile plasticity incorporated with damage parameters is widely adopted due to its versatility and stability in FE simulations, and thus is also adopted in present study. The CDP model requires to specify the constitutive stress-strain relationship for the compressive behavior and tensile behavior, respectively, as well as the corresponding damage characteristics.

Various constitutive models have been developed for normal weight concrete, but very few are for lightweight concrete, especially for fiber-reinforced lightweight concrete. Based on 842 groups of test data, Liu et al. [39] modified an existing model for normal weight concrete

and proposed a general model applicable to both plain lightweight concrete and fiber-reinforced lightweight concrete. Adopting the Weibull distribution for the ascending branch and the log-normal distribution for the descending branch, a statistically stochastic damage constitutive model is derived along with the compressive stress-strain relation, as follows.

$$
\sigma_c = \begin{cases} E_0 \varepsilon_c \exp\left[-\frac{1}{m}\left(\frac{\varepsilon_c}{\varepsilon_{ck}}\right)^m \right] & \varepsilon_c \leq \varepsilon_{ck} \\ f_{ck} \exp\left[-0.5\left(\frac{\ln\left(\frac{\varepsilon_c}{\varepsilon_{ck}}\right)}{n}\right)^2 \right] & \varepsilon_c > \varepsilon_{ck} \end{cases} \tag{1}
$$

and the compressive damage parameter is

$$
d_c = \begin{cases} 1 - \exp\left[-\frac{1}{m}\left(\frac{\varepsilon_c}{\varepsilon_{ck}}\right)^m \right] & \varepsilon_c \leq \varepsilon_{ck} \\ 1 - f_{ck} \exp\left[-0.5\left(\frac{\ln\left(\frac{\varepsilon_c}{\varepsilon_{ck}}\right)}{n}\right)^2 \right] \Big/ E_0 \varepsilon_c & \varepsilon_c > \varepsilon_{ck} \end{cases} \tag{2}
$$

where σ_c and ε_c are the compressive stress and strain, respectively; E_0 is the elastic modulus; f_{ck} is the compressive strength of concrete and ε_{ck} is the corresponding strain at f_{ck}; d_c is the compressive damage parameter; m is the shape factor solved by the boundary conditions at the peak point, and calculated as 2.15 in this study; n is the constant factor determined by curve fitting of the test results, which is 0.883 in this study according to Liu et al.'s recommendation. Based on Eqs. (1) and (2), Figure 2(c) shows the compressive constitutive model in terms of normalized compressive stress and compressive damage parameter defined in the CDP model. The compressive inelastic strain ε_c^{in} is calculated by $\varepsilon_c^{in} = \varepsilon_c - \sigma_c/E_0$ and the normalized compressive stress is the ratio of σ_c/f_{ck}.

The tensile constitutive stress-strain relationships of the LHDCC in the linear elastic stage and the nonlinear strain hardening stage are directly obtained from the averaged tensile coupon test results shown in Figure 2(b). As regards the tensile softening stage, to the authors' best knowledge, no constitutive model has been proposed, specially, for lightweight concrete in the available literature. For normal weight concrete and high strength concrete, a bilinear decay model is proved to be sufficient to represent the stress-strain relationship [40]. Thus, the tensile

softening portion of the LHDCC is also simplified as a bilinear model in this study. Figure 2(d) shows the tensile constitutive model in terms of normalized tensile stress and tensile damage parameter defined in the CDP model. The tensile inelastic strain ε_t^{in} is calculated by $\varepsilon_t^{in} = \varepsilon_t - \sigma_t / E_0$ and the normalized tensile stress is the ratio of σ_t / f_{tu}, where f_{tu} is the ultimate tensile strength.

The CDP model also requires to define dilation angle (w), second stress invariant ratio (K_c), ratio of biaxial to uniaxial compressive strength (r_{b0}/r_{c0}), eccentricity and viscosity factor. Based on previous studies [33, 40, 41] and the calibration with the new test results, these parameters are set as 50°, 0.667, 1.16, 0.1 and 0.0001, respectively.

3.2 Material model of steel

Figures 3(a), (c) and (e) show the engineering stress-strain curves of the 6 mm thickness steel plate, J-hook and headed stud obtained from standard uniaxial tension tests, with the yield strength of around 268 MPa, 326 MPa, and 405 MPa, respectively. All the steel materials follow the isotropic strain hardening law. In ABAQUS, the input of the constitutive model is the true stress-strain relationship, which is derived from the engineering stress-strain according to the equations below.

$$\varepsilon = \ln(1 + e) \tag{3}$$

$$\sigma = S(1 + e) \tag{4}$$

where S and e are the engineering stress and strain, respectively. σ and ε are the true stress and strain, respectively. Figures 3(b), (d) and (f) show the converted true stress-strain relationship of the steel plate, J-hook and headed stud, respectively.

3.3 Element type, mesh scheme, boundary condition

Figure 4 shows the FE model of the double-layer sandwich panel. Due to symmetry, a quarter model is sufficient to represent the whole structure in the FE simulation. All the steel plates, concrete cores, and shear connectors were meshed by the 8-node brick element with reduced integration (C3D8R). The interaction between concrete and steel normally causes convergence problems, especially when concrete damage is included in the model. In order to overcome this issue, all the parts are meshed in the way that a perfect matching mesh is achieved at the contact area. Mesh sensitivity study has been conducted before performing parametric study. The

global mesh size is specified as 10 mm, and the mesh of the shear connector is locally refined with 16 element seeds along the section circumference. The steel plates have 4 elements along the thickness direction and the shear connectors have 4 elements along the length direction. Both the J-hooks and the overlapped headed studs are simplified in the model, the details of which are discussed in Section 3.5. The loading patch and the support rollers are modelled as rigid body. Appropriate boundary conditions are applied on the quarter model to ensure symmetrical deformation of the entire panel. The rollers are fixed and a pressure load is applied on the top surface of the loading patch.

3.4 Contact definition

All the interfacial contacts, including between concrete and steel plate, concrete and shear connector, loading patch and steel plate, and steel plate and roller support, adopt the standard general contact with the indication of surface contact pairs. The two contact surfaces are specified as balanced master-slave relationship, which means that each surface node acts as both master and slave node in the iteration. The balanced master-slave relationship guarantees more accurate contact analysis. The contact properties consist of both normal and tangential properties, with the former specified as hard contact and the latter defined by a friction coefficient. Rabbat and Russell [42] have conducted an experimental investigation to determine the friction coefficient of steel on concrete or grout. The average effective coefficient of static friction varied between 0.57 and 0.70. Most of the current studies determine the friction coefficient between steel and concrete by fitting the test data, and the value ranges from 0.3 to 0.7 [43-45]. Based on these references, as well as the fitting of the test data, the friction coefficient between steel and concrete is also determined as 0.7 in this study. The friction between loading patch and steel plate, and the friction between steel plate and roller support are not sensitive to the results. However, a larger value of friction coefficient would guarantee the stability and convergence of the results in the numerical iteration. Thus, the friction coefficient for steel-to-steel contact is determined as 0.5 in this study.

3.5 Representation of shear connectors

The shear connectors play a significant role in the load transfer mechanism of SCS panels subjected to concentrated punching load. The shear connectors take the transverse shear load

and also prevent longitudinal slip and maintain composite actions between concrete and steel plates. It is found that modelling the geometry of the J-hooks and the overlapped headed studs is very complicated and often causes convergence problems. A simplification approach is proposed in this paper, by which both the J-hooks and the overlapped headed studs are modelled as two steel bars connected by a nonlinear spring element, as shown in Fig. 5. The solid steel bars provide longitudinal shear and flexural resistances, while the nonlinear spring elements provide tensile resistance. The simplified approach requires defining load-displacement curves of the spring elements, which are obtained by testing the SCS units with J-hooks and overlapped studs, respectively.

3.6 Validation of FE model

The current FE model does not incorporate steel damage as serious convergence problems would be caused if both concrete damage and steel damage are incorporated. In this case, punching shear fracture of steel plate is not simulated, and the sandwich structure in the FE analysis only exhibits a linear elastic-nonlinear plastic behavior. Figure 6 compares the load-displacement curves of the single-layer and double layers sandwich specimens between the test results and the ones obtained from FE simulation. Generally, the FE results have a good agreement with the test results before the punching shear fracture of the top steel plate. For most of the specimens, the FE model simulates well the stiffness at the elastic stage, the first peak resistance P_1, and the stiffness at the plastic hardening stage. The non-negligible differences of the load-displacement curves for some of the specimens, like D140-4-S100 and D140-6-S150, can be explained by the following reasons: Firstly, the simplification of shear connectors using nonlinear spring elements introduces deviations on modelling complex interactions between concrete and shear connectors around the connection region, especially in the nonlinear plastic stage. Secondly, the material property of steel plate is obtained based on the coupons extracted from the plain steel plate without shear connectors. However, the welding of shear connectors generates residual stress in the material, which affects the stiffness and ultimate resistance of the steel plate. Thirdly, the crushing and cracks appeared in the concrete core during the loading process are difficult to simulate, which reduces the accuracy of the load-displacement relationship.

Figure 7 compares the failure modes between the test and the FE results for panels D140-6-S100 and D140-6-S150, which have full and partial composite actions, respectively. For D140-6-S100, the shear connectors are sufficient to prevent bond-slip between concrete and steel plates. The panel exhibits significant localized deformation and a punching cone is formed underneath the loading patch. For D140-6-S150, the low degree of composite action leads to obvious bond-slip between concrete and steel plates, which reduces the stresses transferred to the concrete core. The panel exhibits a global flexural deformation accompanied with subsequent localized indentation. The failure modes obtained from the FE results have a good match with those obtained from the test results, as shown in Fig. 7.

4. Parametric Studies

With the validated FE model, a series of parametric studies have been conducted to investigate the sensitivity of geometric and material parameters to the stiffness and load bearing capacity of the double-layer SCS panels. Table 4 lists the parameters considered in the FE simulations, including shear span L_s, concrete height H_c, steel plate thickness t_p, loading patch size a, shear connector spacing S, concrete strength f_{ck} and steel plate strength f_{yp}. The first model in Table 4 serves as the reference model for comparisons, with L_s=500 mm, H_c=140 mm, t_p=6 mm, a=100 mm, S=100 mm, f_{ck}=45 MPa, and f_{yp}=275 MPa.

4.1 Effect of concrete height

Figure 8(a) plots the load-displacement curves of the double-layer SCS panels with the total concrete height varying from 100 mm to 180 mm. The simulations are terminated when the mid-span displacement reaches 75 mm. Figure 8(b) shows the stiffness at elastic and plastic stages, and Fig. 8(c) shows the first peak resistance and the resistance at the displacement of 75 mm for the five specimens with varying concrete height. The first peak resistance and the resistance at the displacement of 75 mm increase with concrete height at almost the same rate. The stiffness at the elastic stage increases with concrete height, while the stiffness at the plastic hardening stage slightly decreases with concrete height, from 12.5 kN/mm to 11.8 kN/mm for the specimen with concrete height ranging from 100 mm to 180 mm. The reason is that at the elastic stage, the panel integrity is well maintained and the higher concrete core ensures larger flexural modulus of the section, thus resulting in larger stiffness of the panel. However, at the

plastic stage, the concrete core fails by punching shear failure at the first peak resistance and the punching cone is formed with the development of critical diagonal cracks. Thus, the contribution of concrete in the plastic stage is significantly reduced. Instead, the stiffness of the panel is mainly contributed by the membrane effect of the steel plates, the size and property of which are the same for the five specimens. The slightly decreasing trend is because more proportion of concrete is cracked for the specimen with larger concrete height. The cracks near the steel plates would cause local bond-slip between steel plates and concrete, which relieves the loading on the steel plates and thus slightly reduces the overall plastic stiffness.

4.2 Effect of shear span

Figure 9 displays the FE results of the double-layer SCS panels with a shear span between two supports varying from 425 mm to 725 mm. Both the stiffness at the elastic and the plastic hardening stages decreases with the shear span. The shear span has limited effects on the first peak resistance and the resistance at the displacement of 75mm. The reason is that the load bearing capacity is mainly determined by the local punching cone. With the increase of displacement, the panel gradually exhibits a local punching shear behavior and fails by punching shear fracture of the top steel plate, which is not sensitive to shear span.

4.3 Effect of steel plate thickness

Figure 10 shows the FE results of the double-layer SCS panels for steel plate thickness of 4 mm, 6 mm, 8 mm and 10 mm. Both the stiffnesses at the elastic stage and the plastic hardening stage increase with the steel plate thickness. For the load bearing capacity, the first peak resistance increases with the steel plate thickness and the increase in resistance is accelerated at the plastic hardening stage, due to the increase in displacement. The resistance at the displacement of 75 mm increases more with the steel plate thickness, as a thicker steel plate has a higher resistance to the external load. In addition, a thicker steel plate provides higher membrane effect of the sandwich panel, especially at the plastic hardening stage.

4.4 Effect of shear connector spacing

Figure 11 shows the FE results of double-layer SCS panels with shear connector spacing varying from 100 mm to 200 mm. The increase of shear connector spacing decreases the stiffness at the elastic stage and has marginal influence on the stiffness at the plastic hardening

stage. For the load bearing capacity, the first peak resistance and the resistance at the displacement of 75 mm decrease with the shear connector spacing almost at the same rate. The reason is that larger shear connector spacing reduces the degree of composite action of SCS panels and the load transfer capacity, and also larger shear connector spacing results in fewer shear connectors in the punching cone to resist the external load. The flat stage after the first peak resistance in Fig. 11(a) is mainly due to the bond-slip between steel plate and concrete. The plastic hardening stage is governed by the membrane action of the top steel plate, that is why the stiffness at this stage is nearly not affected.

4.5 Effect of loading patch size

Figure 12 shows the FE results of double-layer SCS panels with the edge length of loading patch varying from 50 mm to 150 mm. All the three specimens exhibit a local punching cone behavior. Both the stiffnesses at the elastic stage and the plastic hardening stage increase with the loading patch size. The first peak resistance increases with the loading patch size and at the plastic hardening stage the resistance increases slightly faster with the increase of the patch size due to the increased panel displacement. The effect of changing loading patch size can be illustrated as increasing or reducing the volume of the punching cone involved in resisting the external load.

4.6 Effect of concrete strength

Figure 13 exhibits the FE results of double-layer SCS panels with concrete compressive strength varying from 35 MPa to 75 MPa. According to the figure, both the stiffness and the load bearing capacities of SCS panels are not sensitive to concrete strength. The increase of concrete strength only slightly increases the first peak resistances and the rate of increase almost keeps the same at the plastic hardening stage. This phenomenon is well demonstrated in the equation of the first peak resistance by Huang et al. [36], which incorporates concrete compressive strength in the forms of $f_{ck}^{1/3}$ and $f_{ck}^{1/2}$. The exponents 1/3 and 1/2 greatly reduce the effect of concrete strength.

4.7 Effect of steel plate strength

Figure 14 exhibits the FE results of double-layer SCS panels with yield strength of steel plate varying from 235 MPa to 405 MPa. The increase of yield strength does not affect the stiffness

of the panel at the elastic stage, and only slightly increases the first peak resistance, but obviously increases the stiffness and resistance at the plastic hardening stage. The reason is that the first peak resistance is mainly governed by punching shear failure of concrete. The steel plate has not yielded or only a small portion has started to yield at this point. In contrast, at the plastic hardening stage, the behavior of the panel is mainly governed by the membrane action of the top steel plate. The steel plates gradually yield, at the stage of which the yield strength and plastic hardening process of the steel significantly affect the stiffness and resistance of the panel.

5. Analysis on Stiffness and Resistance

Energy absorption ability serves as an important criterion in evaluating the performance of protective sandwich structures. One critical factor related to energy absorption ability is the stiffness or the deformation capacity of the structure. However, numerical simulations of double-layer SCS panels requires expensive computing resources. To reduce this cost, this section aims to develop an analytical model to predict the stiffness at both elastic stage and plastic stages. An idealized load-displacement relationship for double-layer SCS panels is also developed.

5.1 Stiffness at the elastic stage

At the elastic stage, the double-layer SCS panel mainly exhibits a global flexural deformation and the stiffness at this stage is equivalent to the global stiffness of the panel, as shown in Fig. 15. For a simply supported rectangular plate subjected to concentrated load at the center, the global deformation is approximately predicted based on the theory of plates and shells [46]. Assuming the plate with length of L_1 and width of L_2, the global deformation is derived as:

$$\delta_g = \alpha \frac{P L_1^2}{D} = \frac{P}{k_g} \tag{5}$$

where D is the bending stiffness of the plate; the numerical coefficient α depends on the ratio of L_2/L_1. For a square plate with equal value of L_1 and L_2, α is determined as 0.0116 [46]. Replacing L_1 with the span between the two parallel support rollers L ($L=2L_s$), the global deformation stiffness k_g in the current study is derived as:

$$k_g = \frac{D}{0.0116 L^2} \tag{6}$$

The bending stiffness of the panel D is calculated as the sum of the concrete part D_c and the steel plate part D_p. For the double-layer sandwich panel, the concrete part includes the contributions of both the upper and the lower concrete core; the steel plate part includes the contributions of the top, middle and bottom steel plates. The bending stiffness of each part is taken about the neutral axis of the composite section. It should be noted that the double-layer sandwich panels are designed with the same height of the upper and lower concrete cores, as well as the same thickness of the top, middle and bottom steel plates. Therefore, the bending stiffness of the panel, D, the concrete part, D_c, and the steel plate part, D_p, are simplified as,

$$D = D_c + D_p \tag{7}$$

$$D_c = \frac{E_c}{1 - v_c^2} \cdot 2\left[\frac{h_c^3}{12} + h_c\left(\frac{h_c + t_p}{2}\right)^2\right] \tag{8}$$

$$D_p = \frac{E_p}{1 - v_p^2} \cdot \left\{\frac{t_p^3}{12} + 2\left[\frac{t_p^3}{12} + t_p(h_c + t_p)^2\right]\right\} \tag{9}$$

where E_c is elastic modulus of concrete; v_c is Poisson's ratio of concrete; h_c is height of the concrete core; E_p is elastic modulus of steel plate; v_p is Poisson's ratio of steel plate; t_p is thickness of steel plate.

The bending stiffness of the sandwich panel calculated from the above equations assumes that the concrete and the steel plates are perfectly bonded together without slip at the interface, which is always overestimated. In order to quantify the bond effect and take into account bond slip, two FE models specifying the relationship between the concrete surface and steel plate surface as "Tie" constraint and "surface contact" interaction, respectively, are built for each design listed in Table 4. Since only the elastic stage is concerned, all the materials are simplified as elastic. The simulation results listed in Table 5 show that the ratios of the stiffness at the elastic stage for the model using "surface contact" interaction to that using "Tie" constraint vary from 0.11 to 0.29, with an average value of 0.20. To incorporate the effect of partial composite action, a parameter named the degree of composite action η, is introduced. The whole steel plate is divided into four triangular parts in accordance with the loading and boundary conditions, each of which forms a shear span region, as shown in Fig. 16. η is calculated as the ratio of the overall shear strength of the connectors within the shear span region to the tensile strength of the triangular steel plate. Since the triangular plate has variable cross section, the

tensile strength of steel adopts the average cross section of the triangular plate for calculation.

Therefore, half length $L/2$ is used to simplify the degree of composite action η,

$$\eta = \frac{n_s V}{f_{yp} t_p L/2} \leq 1.0 \tag{10}$$

where n_s is the number of shear connectors within the shear span region, or 1/4 of the total number of shear connectors on the steel plate; V is the shear strength of a single headed stud (V_H) or a single J-hook (V_J), calculated according to Eq. (11) [47] and Eq. (12) [48], respectively:

$$V_H = 0.29 \alpha d_H^2 \sqrt{f_{ck} E_c} \leq 0.8 f_{u\_H} A_H \tag{11}$$

$$V_J = 0.855 f_{ck}^{0.265} E_c^{0.469} A_J \left(h_J / d_J\right)^{0.154} \leq 0.8 f_{u\_J} A_J \tag{12}$$

where $\alpha = 0.2(h_H/d_H + 1)$ for $3 \leq h_H/d_H \leq 4$ or $\alpha = 1.0$ for $h_H/d_H > 4$; h_H, d_H, A_H, and f_{u_H} are the overall height, diameter, cross-sectional area, and ultimate strength of the headed stud, respectively; h_J, d_J, A_J, and f_{u_J} are the overall height, diameter, cross-sectional area, and ultimate strength of the J-hook, respectively.

Thus, to consider the effect of partial composite on the stiffness k_g, the bending stiffness is multiplied with a factor of 0.2η, the values of which are very close to the ratios of $k_{g\_contact}/k_{g\_tie}$, as shown in Table 5. Then, the stiffness equation in Eq. (6) is modified as below.

$$k_g = \frac{0.2\eta D}{0.0116 L^2} \tag{13}$$

However, the stiffness equation above is derived with the precondition that the plate is thin (thickness/side length ratio $\xi \leq 0.1$), thus not suitable to be directly applied to the double-layer SCS panel [46], which is normally classified as a thick composite plate. In order to solve this problem, the stiffness equation above requires to be corrected with the influence of the thickness/side length ratio ξ. Table 6 lists the values of the correction factor λ, which equals the ratio of the stiffness calculated according to Eq. (13) to the elastic stiffness obtained from FE, for different values of ξ listed in Table 4, which vary from 0.11 to 0.20. As some of the FE models have the same thickness/side length ratio, the averaged value of the correction factor calculated for these models is adopted here. Figure 17 shows a fitting curve of these scattered points, and the function of the correction factor in relation to the thickness/side length ratio is shown as below.

$$\lambda = -1.65\xi + 0.75 \tag{14}$$

Finally, the stiffness at the elastic stage for double-layer SCS panels is obtained as:

$$k_e = \lambda k_g = \frac{0.2\eta\lambda D}{0.0116L^2} = \frac{\eta\lambda D}{0.058L^2} \tag{15}$$

5.2 Stiffness at the plastic stage

The load bearing mechanism of the double-layer SCS panels at the plastic hardening stage follows the tandem spring model, as shown in Fig. 18. The total deformation δ consists of the global yielding deformation δ_g and the local indentation deformation δ_l, i.e., $\delta = \delta_g + \delta_l$. The external load P has the following relationship with the global and local deformation:

$$P = k_g\delta_g = k_l\delta_l \tag{16}$$

where k_g is the global stiffness calculated from Eq. (15), and k_l is the local stiffness.

The external load P can also be represented in terms of the total deformation as:

$$P = k_p\delta \tag{17}$$

where k_p indicates the stiffness of the sandwich panel at the plastic stage.

According to Eq. (16) and Eq. (17), as well as the relationship between δ, δ_g, and δ_l, the following expression can be obtained:

$$k_p = \frac{k_g k_l}{k_g + k_l} \tag{18}$$

As regards the local deformation stiffness, existing references [49,50] have derived the load-local indentation deformation relationship for simply supported steel plate subjected to a load hammer with hemispherical head.

$$P_s = 4\pi f_{yp} t_p \delta_l \tag{19}$$

where P_s is the load on the steel face plate; f_{yp} is the yield strength of steel plate.

For steel plate subjected to a load hammer with cubic head, the load-local indentation deformation equation can be approximately derived based on the geometric relationship between the two different shapes of hammer. As the ratio between the area of a circle of diameter d and the area of a square of side d is $\pi/4$, the above equation is modified as below for steel plate subjected to cubic hammer.

$$P_s = 16 f_{yp} t_p \delta_l \tag{20}$$

Thus, the local stiffness for a simply supported steel plate is:

$$k_l = 16 f_{yp} t_p \tag{21}$$

As discussed in the above section, the local stiffness equation Eq. (21) requires to be corrected with the influence of the thickness/side length ratio. The same correction factor derived in Eq. (14) is multiplied to the local stiffness.

$$k_l = \lambda \times 16 f_{\text{yp}} t_{\text{p}} = 16 \lambda f_{\text{yp}} t_{\text{p}} \tag{22}$$

Combing Eq. (15), Eq. (18) and Eq. (22), the stiffness at the plastic stage for double-layer SCS panels is obtained as:

$$k_{\text{p}} = \frac{k_{\text{g}} k_l}{k_{\text{g}} + k_l} = \frac{16 \lambda \eta f_{\text{yp}} t_{\text{p}} D}{0.928 f_{\text{yp}} t_{\text{p}} L^2 + \eta D} \tag{23}$$

where D, η and λ are calculated according to Eqs. (7), (10) and (14), respectively.

5.3 Validation of stiffness models

For validation of stiffness model, 8 more test data of double-layer SCS panel are further used indecently. Table 7 and Figure 19 compare the stiffnesses of the 8 double-layer SCS panels listed in Table 1 and 26 models listed in Table 4 between the Test (or FE) results and the predicted results. The proposed stiffness models give very close predictions of both the stiffness at the elastic stage and that at the plastic stage. For the stiffness at the elastic stage, the mean value of the predictive result to Test (FE) result is 1.03 with a standard deviation of 0.12; for the stiffness at the plastic stage, the mean value of the predictive result to Test (FE) result is 0.95 with a standard deviation of 0.13. The comparison validates the accuracy of the proposed stiffness models for double-layer SCS panels.

5.4 Resistances

Huang et al. [36] have developed a punching cone model to predict the three peak resistances of double-layer sandwich panels subjected to concentrated punching load. The three peak resistances of the load-displacement curve are caused by punching shear failure of concrete, punching shear fracture of the top steel plate, and punching shear fracture of the middle steel plate, respectively. Whether there is bond-slip failure between the concrete and steel plates depends on the degree of composite action. Among these three peak resistances, the first and the second peak resistances serve as the lower and upper bounds of the load bearing capacity in the design of double-layer sandwich panels, and thus are more critical.

In the punching cone model, the first peak resistance P_1 consists of the contributions from the concrete in the upper and lower layers, V_{c1} and V_{c2}, from the shear connectors in the upper and lower layers, V_{s1} and V_{s2}, and from the top steel plate, V_{pt}. Hence,

$$P_1 = V_c + V_s + V_{pt} = V_{c1} + V_{c2} + V_{s1} + V_{s2} + 0.33\sqrt{f_{ck}}\frac{E_p}{E_c}S_t t_p \qquad (24)$$

where S_t is the perimeter of the loading patch.

At the second peak resistance P_2, the concrete punching cone has already developed with critical diagonal cracks and the concrete is considered ineffective in resisting the punching load. The second peak resistance, therefore, consists of the contributions from the shear connectors in the upper and lower layers, V_{s1} and V_{s2}, from the top steel plate, V_{pt}, and from the middle steel plate, V_{pm}. In addition, the degree of composite action η is incorporated in the resistance model to reflect the bond-slip effect.

$$P_2 = V_s + V_{pt} + V_{pm} = V_{s1} + V_{s2} + S_t t_p \frac{f_{up}}{\sqrt{3}} + \eta S_m t_p \frac{f_{yp}}{\sqrt{3}} \qquad (25)$$

where, S_m is the perimeter of the intersection between the punching cone and the middle steel plate. The detailed explanations on the calculation of V_{c1}, V_{c2}, V_{s1} and V_{s2} in Eq. (24) and (25) refer to Huang et al. [36].

5.5 Idealized load-displacement model

After the stiffnesses at both the elastic and plastic hardening stages and the first two peak resistances are determined, the load-displacement curve for double-layer sandwich panels under concentrated punching load can be approximately defined as a four-stage polyline model, as shown in Fig 20. After the load reaches P_1, the plateau until δ_1' is attributed to punching shear failure of concrete and bond-slip between concrete and steel. According to the test and FE results, a partial composite panel exhibits longer plateau than a full composite panel. Based on Japanese code JEAG 4618-2005 [51] for SC structures, the reduction factor for the stiffness of partial composite design of SC structures is designed as $\sqrt{\eta'} = \sqrt{n_p/n_f}$, in which n_p and n_f are the number of shear connectors arranged and the number of shear connectors required, respectively. To consider the effect of composite action, δ_1' is expressed as $\delta_1' = \delta_1/\sqrt{\eta'}$ in the current study. After the load reaches P_2, the panel is failed by punching shear fracture of the top steel plate and the load-displacement curve drops quickly with a significant loss of

loading capacity. Although in the test the load continues to increase due to the membrane action of the middle steel plate, this branch is not included in the idealized load-displacement curve for conservative consideration. Figure 21 compares the load-displacement curves among the test results, FE results and prediction results. The good match proves that the idealized load-displacement model provides an efficient approach to predict the elastic and nonlinear plastic behavior of double-layer SCS panels under concentrated punching load. The four-stage polyline model can serve as an effective way to evaluate energy absorption ability in the dynamic analysis of double layer SCS panels in the future research.

6. Conclusions

Both experimental and numerical investigations have been performed to study a newly developed double-layer steel-LHDCC-steel sandwich panel under concentrated punching load. Parametric analyses were carried out to assess the effects of concrete height, shear span, steel plate thickness, shear connector spacing, loading patch size, concrete strength and steel plate strength on the stiffness and load resistance of the panel. Finally, analytical models for predicting the stiffness of the panel at elastic and plastic stages were respectively developed, and an idealized load-displacement model for the double-layer SCS panel was also proposed. The following conclusions are drawn from the study.

(1) The punching cone model has successfully illustrated the load transfer mechanism of the double-layers SCS panel under concentrated punching load. The concrete core provides a greater contribution to the stiffness and load resistance of the panel before punching shear failure of concrete. After that, load bearing capacity of the concrete is significantly reduced and the structural performance of the panel is mainly governed by the membrane action of the steel plates. For the SCS panel with partial composite action, global deformation due to bond-slip is also evident.

(2) Both the stiffness at elastic stage (k_e) and the stiffness at plastic stage (k_p) are sensitive to shear span, steel plate thickness, and loading patch size. In addition, the stiffness at elastic stage is sensitive to concrete height and shear connector spacing, while the stiffness at plastic stage is sensitive to steel plate strength. The concrete strength has limited effect on both stiffnesses.

(3) Both the first peak resistance (P_1) and the resistance at the end of the simulation ($P_{\delta=75mm}$) are sensitive to concrete height, steel plate thickness, shear connector spacing, and loading patch size. Shear span and concrete strength have limited effects on both resistances. yield strength of the steel plate has obviously positive effect on the resistance at the end of the simulation, although the influence on the first peak resistance is relatively smaller.

(4) The proposed stiffness models for double-layer SCS panels have incorporated all the factors discussed in the parametric analyses, and provide a simple and effective method to calculate both the stiffness at both elastic and plastic stages. The validations against FE results show that the stiffness models are sufficiently accurate.

(5) The idealized four-stage polyline load-displacement model provides a convenient approach to predict deformation and load bearing capacity of the double-layer SCS panels subjected to concentrated punching load, and may serve as an effective way to evaluate energy absorption ability of the panel in dynamic analysis.

Acknowledgement

Nomenclature	
a	Edge length of loading patch
f_{ck}	Strength of concrete cylinder in compression
f_{yp}, f_{up}	Yield strength and ultimate strength of steel plate, respectively
f_{y_J}, f_{u_J}	Yield strength and ultimate strength of J-hook, respectively
f_{y_H}, f_{u_H}	Yield strength and ultimate strength of headed stud, respectively
h_{c1}	Height of upper concrete core
h_{c2}	Height of lower concrete core
k_e	Stiffness at the elastic stage

k_g	Global deformation stiffness
k_l	Local deformation stiffness
k_p	Stiffness at the plastic stage
m_f	Flexural resistance of the panel per unit length
t_p	Thickness of steel plate
D	Bending stiffness
D_c	Bending stiffness contributed by concrete
D_p	Bending stiffness contributed by steel plate
E_c	Elastic modulus of concrete
E_p	Elastic modulus of steel plate
H_c	Total height of concrete core ($H_\mathrm{c} = h_{\mathrm{c}1} + h_{\mathrm{c}2}$)
L	Span between the two parallel support rollers
L_s	Shear span from the loading patch to the support roller
P	Concentrated load applied on the panel
P_1, P_2, P_3	Resistance at the first, second, and third peak, respectively
S	Spacing between two adjacent shear connectors
S_t	Perimeter of the loading patch
$V_{\mathrm{c}1}, V_{\mathrm{c}2}$	Resistance contributed by upper and lower concrete core, respectively
V_c	Resistance contributed by concrete ($V_\mathrm{c} = V_{\mathrm{c}1} + V_{\mathrm{c}2}$)
$V_\mathrm{pt}, V_\mathrm{pm}$	Resistance contributed by top and middle steel plate, respectively
$V_{\mathrm{s}1}, V_{\mathrm{s}2}$	Resistance contributed by shear connectors in the upper and lower layer, respectively
V_s	Resistance contributed by shear connectors ($V_\mathrm{s} = V_{\mathrm{s}1} + V_{\mathrm{s}2}$)
δ	Total deformation
δ_g	Global deformation
δ_l	Local indentation deformation
η	Degree of composite action
ε_c	Compressive strain
ε_ck	Corresponding compressive strain at f_ck
σ_c	Compressive stress

| v_c | Poisson's ratio of concrete |
| v_p | Poisson's ratio of steel plate |

References

[1] Liew JR, Sohel K. Structural performance of steel-concrete-steel sandwich composite structures. Advances in Structural Engineering 2010; 13: 453-70.

[2] Liew JR, Yan JB, Huang ZY. Steel-concrete-steel sandwich composite structures-recent innovations. Journal of Constructional Steel Research 2017; 130: 202-21.

[3] Zhao XL, Han LH. Double skin composite construction. Progress in structural engineering and materials 2006; 8(3): 93-102.

[4] Bowerman H, Coyle N, and Chapman J. An innovative steel/concrete construction system. Structural Engineer 2002; 80(20): 33-38.

[5] Liew JR, Yan JB, and Huang ZY. Steel-concrete-steel sandwich composite structures-recent innovations. Journal of Constructional Steel Research 2017; 130: 202-221.

[6] Huang ZY, Liew JR, Xiong M, Wang J. Structural behaviour of double skin composite system using ultra-lightweight cement composite. Construction and Building Materials 2015; 86: 51-63.

[7] Liew JR, Sohel KMA, and Koh C. Impact tests on steel–concrete–steel sandwich beams with lightweight concrete core. Engineering Structures 2009; 31(9): 2045-2059.

[8] Guo Q, Zhao W. Design of steel-concrete composite walls subjected to low-velocity impact. Journal of Constructional Steel Research 2019; 154: 190-196.

[9] Wang Y, Liew JR, Lee SC. Experimental and numerical studies of non-composite Steel–Concrete–Steel sandwich panels under impulsive loading. Materials & Design 2015; 81: 104-112.

[10] Yan C, Wang Y, Zhai X, et al. Experimental study on curved steel-concrete-steel sandwich shells under concentrated load by a hemi-spherical head. Thin-Walled Structures 2019; 137: 117-128.

[11] Huang ZY and Liew JR, Compressive resistance of steel-concrete-steel sandwich composite walls with J-hook connectors. Journal of Constructional Steel Research 2016; 124: 142-162.

[12] Yang G, Wang G, Lu W, et al. Experimental and numerical study of damage characteristics of RC slabs subjected to air and underwater contact explosions. Marine Structures 2019; 66: 242-257.

[13] Leng YB, Song XB, and Wang HL. Failure mechanism and shear strength of steel–concrete–steel sandwich deep beams. Journal of Constructional Steel Research 2015; 106: 89-98.

[14] Wang Y, Liew JR, Lee SC. Ultimate strength of steel–concrete–steel sandwich panels under lateral pressure loading. Engineering Structures 2016; 115: 96-106.

[15] Sohel KMA, Liew JYR, Koh CG. Numerical modelling of lightweight Steel-Concrete-Steel

sandwich composite beams subjected to impact. Thin-Walled Structures 2015; 94: 135-146.

[16] Jiang D, Tan KH, Wang CM, et al. Analysis and design of floating prestressed concrete structures in shallow waters. Marine Structures 2018; 59: 301-320.

[17] Yan JB, Liu XM, Liew JR, et al. Steel–concrete–steel sandwich system in Arctic offshore structure: Materials, experiments, and design. Materials & Design 2016; 91: 111-121.

[18] Ellis RM, Macgregor JG. Tests on arch-shaped ice-resisting walls for offshore structures. Structural Journal 1993; 90(1): 42-51.

[19] Palmer A, Croasdale K. Arctic offshore engineering. World Scientific Publishing Co. Pte. Ltd, 5 Toh Tuck Link, Singapore, 2013.

[20] Guo YT, Tao MX, Nie X, et al. Experimental and theoretical studies on the shear resistance of steel–concrete–steel composite structures with bidirectional steel webs. Journal of Structural Engineering 2018; 144(10): 04018172.

[21] Kuo W, Cheng T, and Hwang S. Force transfer mechanism and shear strength of reinforced concrete beams. Engineering Structures 2010; 32(6): 1537-1546.

[22] Leng YB and Song XB. Experimental study on shear performance of steel–concrete–steel sandwich beams. Journal of Constructional Steel Research 2016; 120: 52-61.

[23] Sener KC, Varma AH, and Seo J. Experimental and numerical investigation of the shear behavior of steel-plate composite (SC) beams without shear reinforcement. Engineering Structures 2016; 127: 495-509.

[24] Qin F, Tan S, Yan J, et al. Minimum shear reinforcement ratio of steel plate concrete beams. Materials and structures 2016; 49(9): 3927-3944.

[25] Eurocode 2, Eurocode 2: Design of concrete structures: Part 1-1: General rules and rules for buildings. 2004: British Standards Institution.

[26] ACI 349M. Code Requirements for Nuclear Safety-related Concrete Structures:(ACI 349-06) and Commentary, an ACI Standard. 2006. American Concrete Institute.

[27] Lin Y, Yan J, Wang Y, et al. Shear failure mechanisms of SCS sandwich beams considering bond-slip between steel plates and concrete. Engineering Structures 2019; 181: 458-475.

[28] Zhang W, Huang Z, Fu Z, et al. Shear resistance behavior of partial composite Steel-Concrete-Steel sandwich beams considering bond-slip effect. Engineering Structures 2020; 210: 110394.

[29] Sohel K, Liew JR. Steel–Concrete–Steel sandwich slabs with lightweight core—Static performance. Engineering structures 2011; 33: 981-92.

[30] Shanmugam NE, Kumar G, Thevendran V. Finite element modelling of double skin composite slabs. Finite elements in analysis and design 2002; 38(7): 579-599.

[31] Leng YB, Song XB. Flexural and shear performance of steel-concrete-steel sandwich slabs under concentrate loads. Journal of Constructional Steel Research 2017; 134: 38-52.

[32] Yan C, Wang Y, Zhai X, et al. Experimental study on curved steel-concrete-steel sandwich shells under concentrated load by a hemi-spherical head. Thin-Walled Structures 2019; 137: 117-128.

[33] Huang ZY, Liew JR. Nonlinear finite element modelling and parametric study of curved steel–concrete–steel double skin composite panels infilled with ultra-lightweight cement composite. Construction and Building Materials 2015; 95: 922-38.

[34] Wang Y, Zhai X, Lee SC, et al. Responses of curved steel-concrete-steel sandwich shells subjected to blast loading. Thin-Walled Structures 2016; 108: 185-92.

[35] Huang ZY, Wang JY, Liew JR, et al. Lightweight steel–concrete–steel sandwich composite shell subject to punching shear. Ocean Engineering 2015; 102: 146-61.

[36] Huang ZY, Zhao XL, Zhang W, et al. Load Transfer Mechanism of Novel Double-layer Steel-LHDCC-Steel Sandwich Panels under Punching Loads. Engineering Structures, 2021; 226, 111427.

[37] Huang ZY, Deng WX, Du SL, et al. Effect of Rubber Particles and Fibers on the Dynamic Compressive Behavior of Novel Ultra-lightweight Cement Composites: Numerical simulations and Metamodeling. Composite Structures, 2020; 113210.

[38] Huang ZY, Sui LL, Wang F, et al. Dynamic compressive behavior of novel ultra-lightweight cement composite incorporated with rubber powder. Composite Structures. 2020; 29: 112300.

[39] Liu X, Wu T, Liu Y. Stress-strain relationship for plain and fibre-reinforced lightweight aggregate concrete. Construction and Building Materials 2019; 225: 256-272.

[40] Zhang W, Choo YS, Feng L, et al. Representation of nonlinear behavior of fully grouted K joints in pushover analysis. Journal of Constructional Steel Research 2020; 169: 106024.

[41] Zhang W, Choo YS, Yang P, et al. Nonlinear behaviour of fully grouted CHS X joints and associated representation for overall frame analysis. Thin-Walled Structures 2020; 152: 106761.

[42] Rabbat BG, Russell HG. Friction coefficient of steel on concrete or grout. Journal of Structural Engineering 1985; 111(3):505-515.

[43] Ding F, Zhang T, Liu X, et al. Behavior of steel-reinforced concrete-filled square steel tubular stub columns under axial loading. Thin-Walled Structures 2017; 119: 737-748.

[44] Dai Z, Dai Pang S, Liew J Y R. Axial load resistance of grouted sleeve connection for modular construction. Thin-Walled Structures 2020; 154: 106883.

[45] Chen T, Cao C, Zhang C, et al. Numerical modeling and parametric analysis of grouted connections under axial loading. Thin-Walled Structures 2020; 154: 106880.

[46] Timoshenko SP, Woinowsky-Krieger S. Theory of plates and shells. McGraw-hill 1959.

[47] Eurocode 4. Design of Composite Steel and Concrete Structures Part 1.1: General Rules and Rules for Buildings. Thomas Telford 2004.

[48] Yan JB, Liew JR, Sohel KMA, et al. Push-out tests on J-hook connectors in steel–concrete–steel sandwich structure. Materials and structures 2014; 47: 1693-714.

Draft, 1/22/2022

[49] Guo Q, Zhao W. Displacement response analysis of steel-concrete composite panels subjected to impact loadings. International Journal of Impact Engineering 2019; 131: 272-281.

[50] Sohel KMA, Liew JR. Behavior of steel–concrete–steel sandwich slabs subject to impact load. Journal of Constructional Steel Research 2014; 100: 163-175.

[51] JEAG 4618-2005. Technical guidelines for aseismic design of steel plate reinforced concrete structures-buildings and structures. Tokyo, Japan: Japan Electric Association Nuclear Standards Committee; 2005.

Table 1: Geometric parameters and material properties of SCS panels tested by the authors [36].

Specimen	L_s (mm)	h_{c1} (mm)	h_{c2} (mm)	H_c (mm)	t_p (mm)	a (mm)	S (mm)	Concrete	Steel plate		J-hook		Headed stud	
								f_{ck} (MPa)	f_{yp} (MPa)	f_{up} (MPa)	f_{y_J} (MPa)	f_{u_J} (MPa)	f_{y_H} (MPa)	f_{u_H} (MPa)
S90-6	500	90	/	90	6	100	100	44.3	268	418	326	444	405	509
S140-6	500	140	/	140	6	100	100	43.3	268	418	326	444	405	509
D140-4	500	70	70	140	4	100	100	42.9	272	428	326	444	405	509
D140-6	500	70	70	140	6	100	100	44.2	268	418	326	444	405	509
D140-8	500	70	70	140	8	100	100	44.9	262	394	326	444	405	509
D140-6(J)	500	70	70	140	6	100	100	43.9	268	418	326	444	/	/
D140-6(H)	500	70	70	140	6	100	100	42.6	268	418	/	/	405	509
D140-6(S150)	500	70	70	140	6	100	150	44.3	268	418	326	444	405	509
D140-6(S200)	500	70	70	140	6	100	200	45.0	268	418	326	444	405	509
D140-6(A150)	500	70	70	140	6	150	100	44.6	268	418	326	444	405	509

Notes: L_s is the shear span from the loading patch to the support roller; h_{c1} is the height of upper concrete core; h_{c2} is the height of lower concrete core; H_c is the total height of concrete core; t_p is the thickness of steel plate; a is the width of the loading patch; S is the spacing between the two adjacent connectors; f_{ck} is the compressive cylinder strength of concrete (MPa); f_{yp}, f_{up} are the yield and ultimate strength of steel plate; f_{y_J}, f_{u_J} are the yield and ultimate strength of J-hook; f_{y_H}, f_{u_H} are the yield and ultimate strength of headed stud.

Table 2: Mix proportion of LHDCC (kg/m3)

	Water	OPC	SF	GGBFS	PE fiber	HWRA	SRA
LHDCC	259.0	702.0	78.0	339.9	9.7	7.0	9.0

Notes: OPC=ordinary Portland cement; SF=silica fume; GGBFS= ground granulated blast furnace slag; HWRA=high Water reducing agent; SRA=shrinkage reducing agent.

Table 3 Mechanical properties of the surface treated PE fiber.

Diameter (μm)	Length (mm)	Density (g/cm³)	Tensile strength (MPa)	Elastic modulus (GPa)	Fracture elongation (%)
24	12	0.97	3000	120	2-3

Draft, 1/22/2022

Table 4: FE models in the parametric study

FE models	L_s (mm)	H_c (mm)	t_p (mm)	a (mm)	S (mm)	ξ	η	f_{ck} (MPa)	f_{yp} (MPa)
SP-Reference	500	140	6	100	100	0.16	1.00	45	275
SP-L425	425	140	6	100	100	0.19	1.00	45	275
SP-L575	575	140	6	100	100	0.14	1.00	45	275
SP-L650	650	140	6	100	100	0.12	1.00	45	275
SP-L725	725	140	6	100	100	0.11	1.00	45	275
SP-H100	500	100	6	100	100	0.12	1.00	45	275
SP-H120	500	120	6	100	100	0.14	1.00	45	275
SP-H160	500	160	6	100	100	0.18	1.00	45	275
SP-H180	500	180	6	100	100	0.20	1.00	45	275
SP-t4	500	140	4	100	100	0.15	1.00	45	275
SP-t8	500	140	8	100	100	0.16	1.00	45	275
SP-t10	500	140	10	100	100	0.17	1.00	45	275
SP-a50	500	140	6	50	100	0.16	1.00	45	275
SP-a150	500	140	6	150	100	0.16	1.00	45	275
SP-S125	500	140	6	100	125	0.16	0.83	45	275
SP-S150	500	140	6	100	150	0.16	0.65	45	275
SP-S175	500	140	6	100	175	0.16	0.51	45	275
SP-S200	500	140	6	100	200	0.16	0.37	45	275
SP-fc35	500	140	6	100	100	0.16	1.00	35	275
SP-fc55	500	140	6	100	100	0.16	1.00	55	275
SP-fc65	500	140	6	100	100	0.16	1.00	65	275
SP-fc75	500	140	6	100	100	0.16	1.00	75	275
SP-fp235	500	140	6	100	100	0.16	1.00	45	235
SP-fp355	500	140	6	100	100	0.16	1.00	45	355
SP-fp420	500	140	6	100	100	0.16	1.00	45	420
SP-fp460	500	140	6	100	100	0.16	1.00	45	460

Notes: "SP-Reference" indicates the reference model; "SP-L425" indicates model with L_s=425 mm; "SP-H100" indicates model with H_c =100mm; "SP-t4" indicates model with t_p =4mm; "SP-a50" indicates model with a=50mm; "SP-S125" indicates model with S=125mm; "SP-fc35" indicates model with f_{ck}=35MPa; "SP-fp235" indicates model with f_{yp}=235MPa; $\xi=(H_c+3t_p)/(2L_s)$ is the thickness/side length ratio; η is the degree of composite action and illustrated in Section 5.1.

Draft, 1/22/2022

Table 5: Comparison of k_g between the model using "Tie" constraint and the model using "Surface contact"

Specimen	k_{g_tie} (kN/mm)	$k_{g\_contact}$ (kN/mm)	$k_{g\_contact}$/ k_{g_tie}	0.2η
SP-Reference	851.4	163.3	0.18	0.20
SP-L425	876.0	185.5	0.21	0.20
SP-L575	596.8	133.2	0.22	0.20
SP-L650	508.7	110.1	0.22	0.20
SP-L725	416.5	96.6	0.23	0.20
SP-H100	476.1	87.6	0.18	0.20
SP-H120	614.5	124.5	0.20	0.20
SP-H160	837.6	203.3	0.24	0.20
SP-H180	959.7	278.1	0.29	0.20
SP-t4	672.2	120.7	0.19	0.20
SP-t8	988.8	190.6	0.19	0.20
SP-t10	983.0	222.7	0.23	0.20
SP-a50	540.2	145.3	0.27	0.20
SP-a150	899.0	186.9	0.21	0.20
SP-S125	742.9	110.4	0.15	0.17
SP-S150	747.8	105.4	0.14	0.13
SP-S175	737.6	81.6	0.11	0.10
SP-S200	752.4	75.9	0.10	0.07
SP-fc35	851.4	160.9	0.19	0.20
SP-fc55	851.4	164.8	0.19	0.20
SP-fc65	851.4	166.1	0.20	0.20
SP-fc75	851.4	168.3	0.20	0.20
SP-fp235	851.4	162.9	0.19	0.20
SP-fp355	851.4	165.0	0.19	0.20
SP-fp420	851.4	168.6	0.20	0.20
SP-fp460	851.4	169.0	0.20	0.20

Table 6: Correction to thickness/side length ratio for FE models

ξ	λ
0.11	0.60
0.12	0.53
0.14	0.52
0.15	0.52
0.16	0.49
0.17	0.39
0.18	0.46
0.19	0.40
0.20	0.49

Table 7: Comparison of stiffnesses at the elastic stage and plastic hardening stage between Test (or FE) and prediction model

Test models	k_e			k_p		
	Test (kN/mm)	Pred (kN/mm)	Pred/Test	Test (kN/mm)	Pred (kN/mm)	Pred/Test
D140-4	101.0	117.4	1.16	13.6	8.2	0.60
D140-6	155.2	163.3	1.05	15.1	11.9	0.79
D140-8	155.7	217.9	1.40	22.2	15.8	0.71
D140-6(J)	138.8	163.3	1.18	14.2	11.9	0.84
D140-6(H)	158.4	163.3	1.03	13.8	11.9	0.86
D140-6(S150)	86.2	105.5	1.22	10.7	11.5	1.07
D140-6(S200)	70.9	59.8	0.84	11.6	10.6	0.91
D140-6(A150)	154.4	163.3	1.06	16.4	11.9	0.73
FE models	FE (kN/mm)	Pred (kN/mm)	Pred/FE	FE (kN/mm)	Pred (kN/mm)	Pred/FE
SP-Reference	163.3	163.3	1.00	12.2	11.9	0.97
SP-L425	185.5	203.0	1.09	13.2	10.9	0.83
SP-L575	133.2	131.8	0.99	12.9	12.5	0.97
SP-L650	110.1	109.7	1.00	11.3	12.9	1.14
SP-L725	96.6	90.8	0.94	11.1	12.8	1.16
SP-H100	87.6	94.9	1.08	12.5	12.6	1.01
SP-H120	124.5	127.8	1.03	12.3	12.5	1.01
SP-H160	203.3	200.4	0.99	12.0	11.3	0.94

SP-H180	278.1	238.0	0.86	11.8	10.6	0.90
SP-t4	120.7	117.4	0.97	7.2	8.2	1.14
SP-t8	190.6	217.9	1.14	15.3	15.8	1.04
SP-t10	222.7	268.2	1.20	19.4	19.2	0.99
SP-a50	145.3	163.3	1.12	10.1	11.9	1.17
SP-a150	186.9	163.3	0.87	14.6	11.9	0.81
SP-S125	110.4	134.3	1.22	12.8	11.7	0.91
SP-S150	105.4	105.5	1.00	12.3	11.5	0.93
SP-S175	81.6	82.6	1.01	12.7	11.1	0.87
SP-S200	75.9	59.8	0.79	12.1	10.6	0.88
SP-fc35	160.9	163.3	1.01	12.1	11.9	0.98
SP-fc55	164.8	163.3	0.99	12.2	11.9	0.97
SP-fc65	166.1	163.3	0.98	12.2	11.9	0.97
SP-fc75	168.3	163.3	0.97	12.3	11.9	0.96
SP-fp235	162.9	163.3	1.00	9.6	10.3	1.08
SP-fp355	165.0	163.3	0.99	15.5	15.1	0.97
SP-fp420	168.6	163.3	0.97	18.0	18.5	1.03
SP-fp460	169.0	163.3	0.97	19.5	20.1	1.03
Mean			1.03			0.95
Std.Dev			0.12			0.13

Author Statement

Wei ZHANG: Writing-Reviewing and Editing;
Zhenyu HUANG: Conceptualization, Methodology, Funding Acquisition, Supervision; Writing- Reviewing and Editing;
Jianqiao Ye: Methodology, Writing- Reviewing and Editing;
Youtam: Investigation, Writing and Editing.

- ➢ Perform experimental and numerical investigations to study the punching behavior of sandwich panel.
- ➢ Perform parametric analyses on the stiffness and load resistance of the panel.
- ➢ Develop analytical models for predicting the stiffness of the panel at elastic and plastic stages.
- ➢ Propose an idealized load-displacement model for the sandwich panel.

(a) Test set-up and loading scheme

(b) Failure mode of D140-4-S100

(c) Failure mode of D140-6-S150
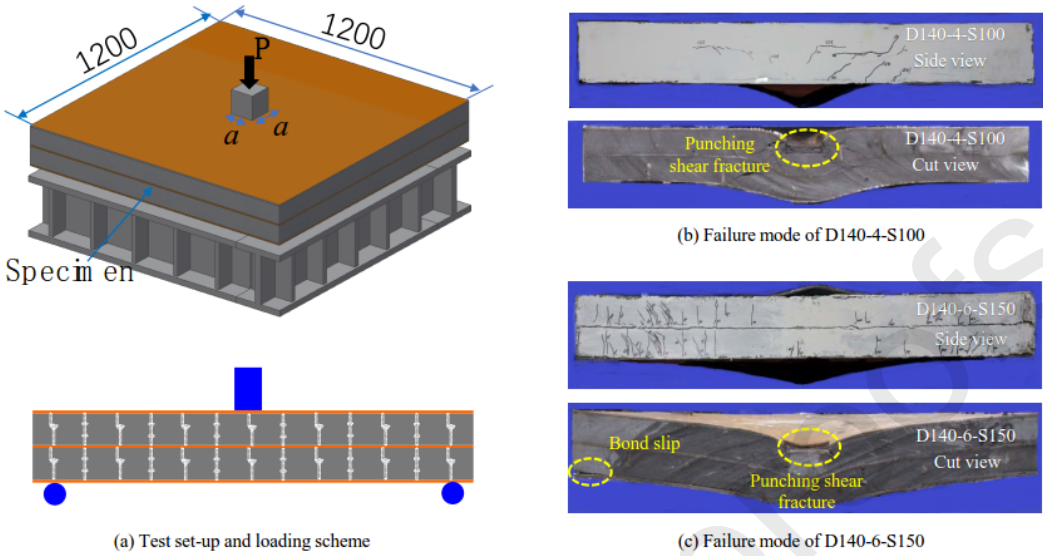
Figure 1 Experimental program

(a) Compressive stress-strain curve by test

(b) tensile stress-strain curve by test

(c) Compressive constitutive model in FE

(d) Tensile constitutive model in FE
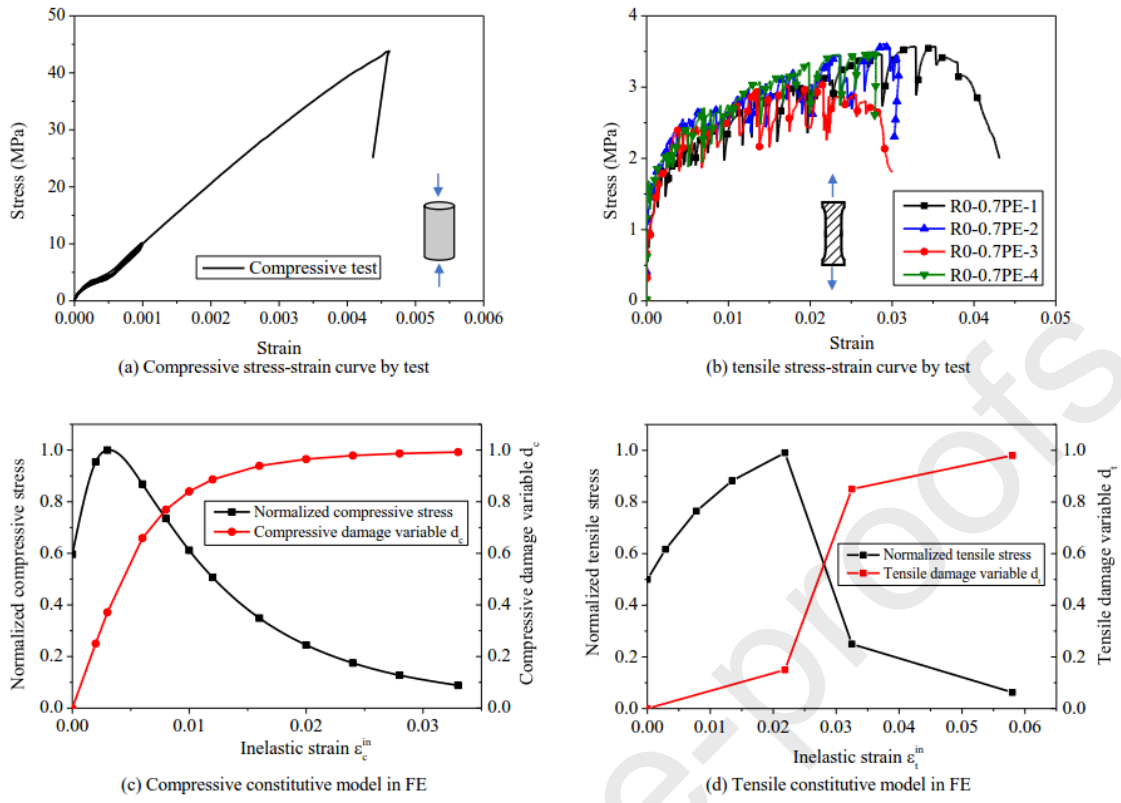
Figure 2 Material property of concrete

(a) 6 mm steel plate by test

(b) 6 mm steel plate in FE

(c) J-hook by test

(d) J-hook in FE

Figure 3 Material property of steel

(e) Headed stud by test

(f) Headed stud in FE
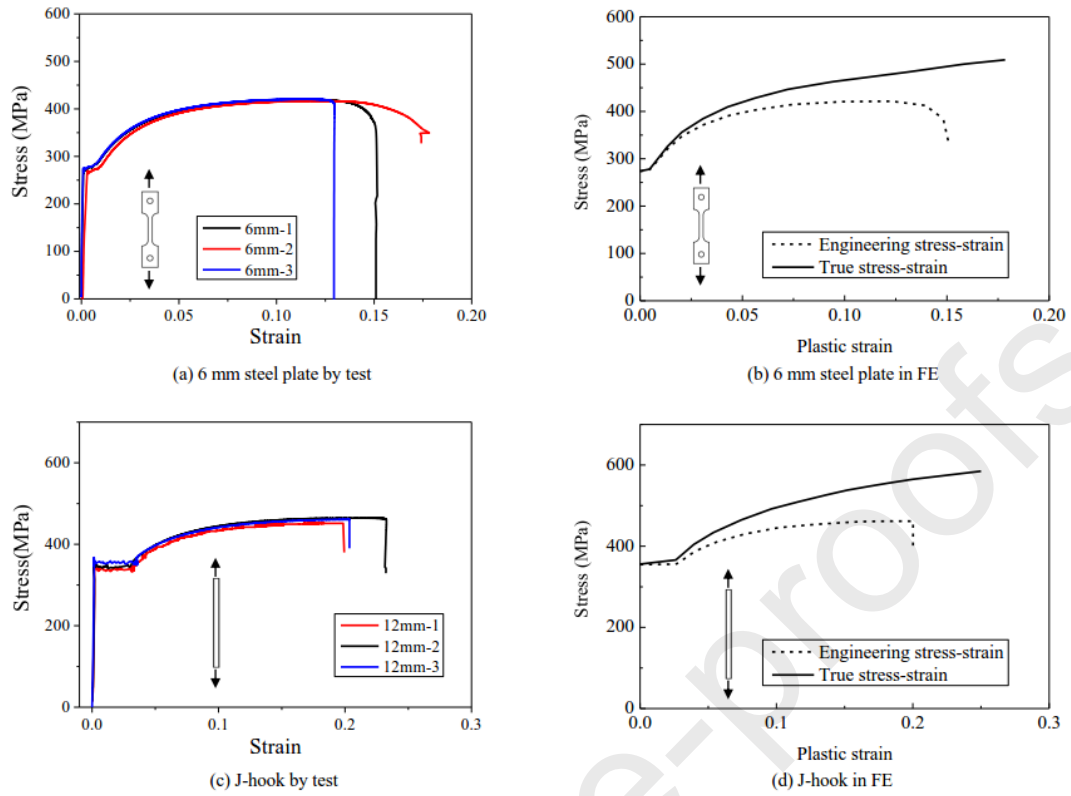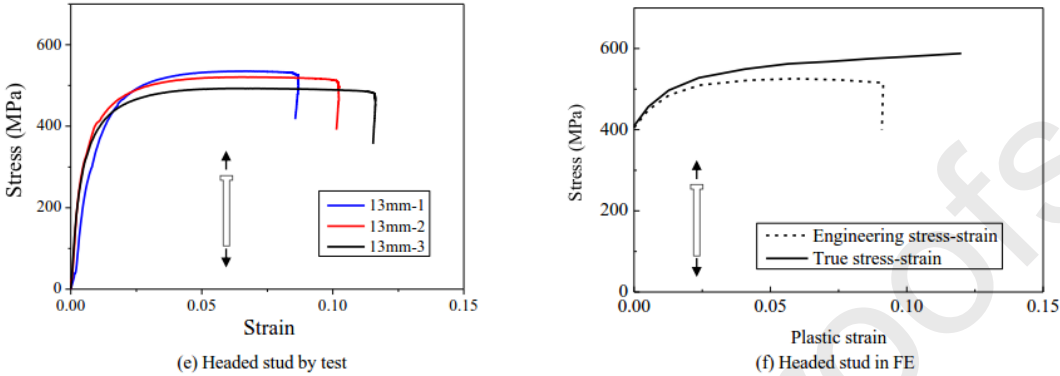
Figure 3 Material property of steel
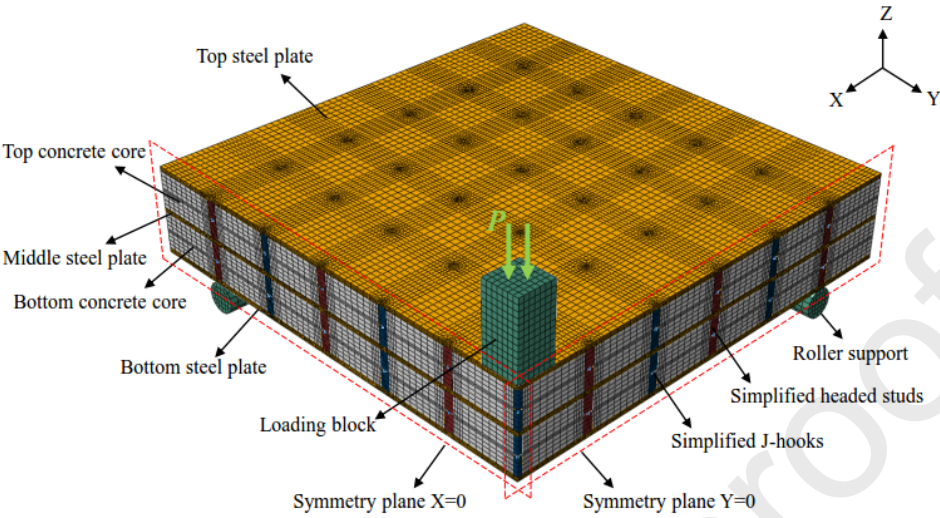
Figure 4 FE model of double-layer sandwich panel

(a) J-hooks

(b) Overlapped headed studs
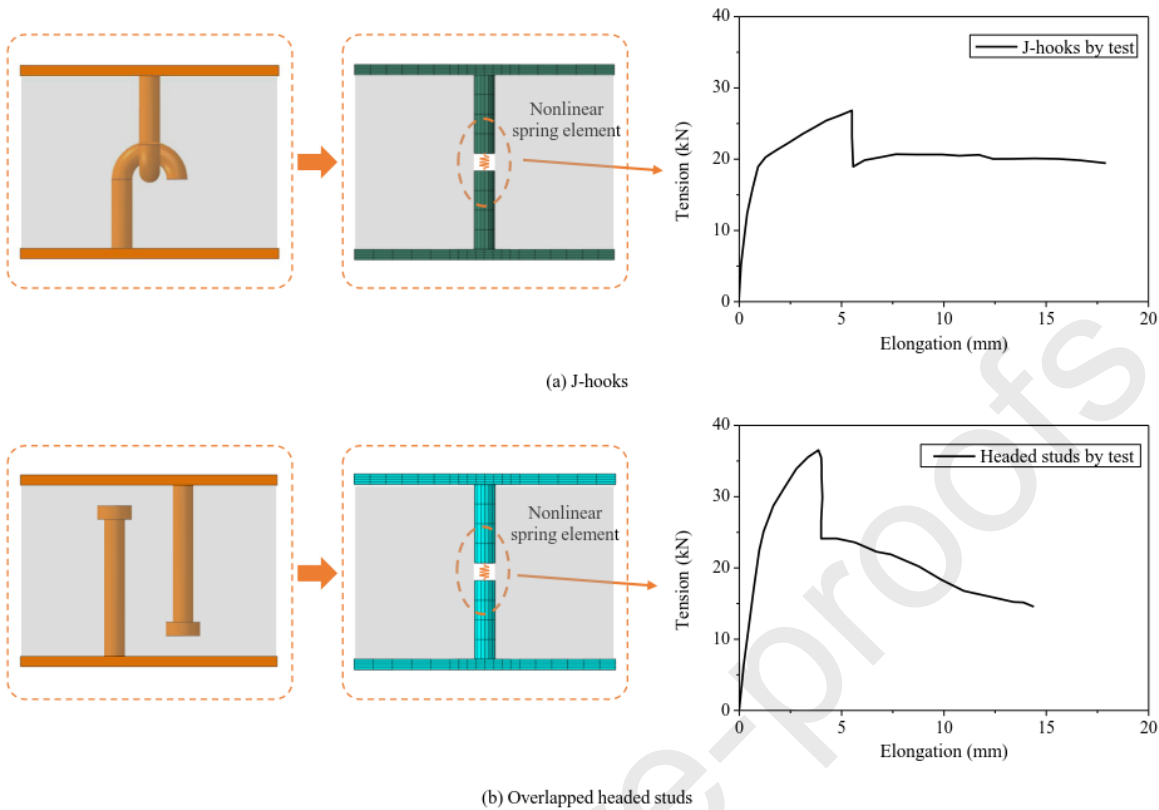
Figure 5 Simplification of J-hooks and overlapped headed studs
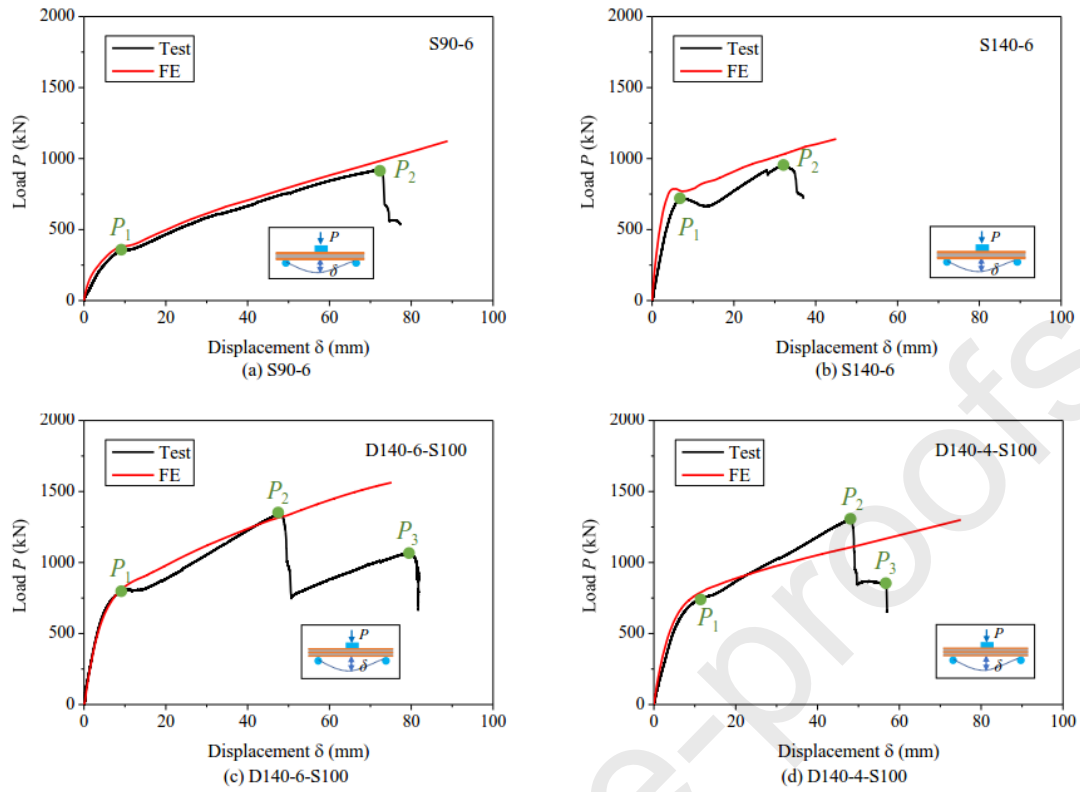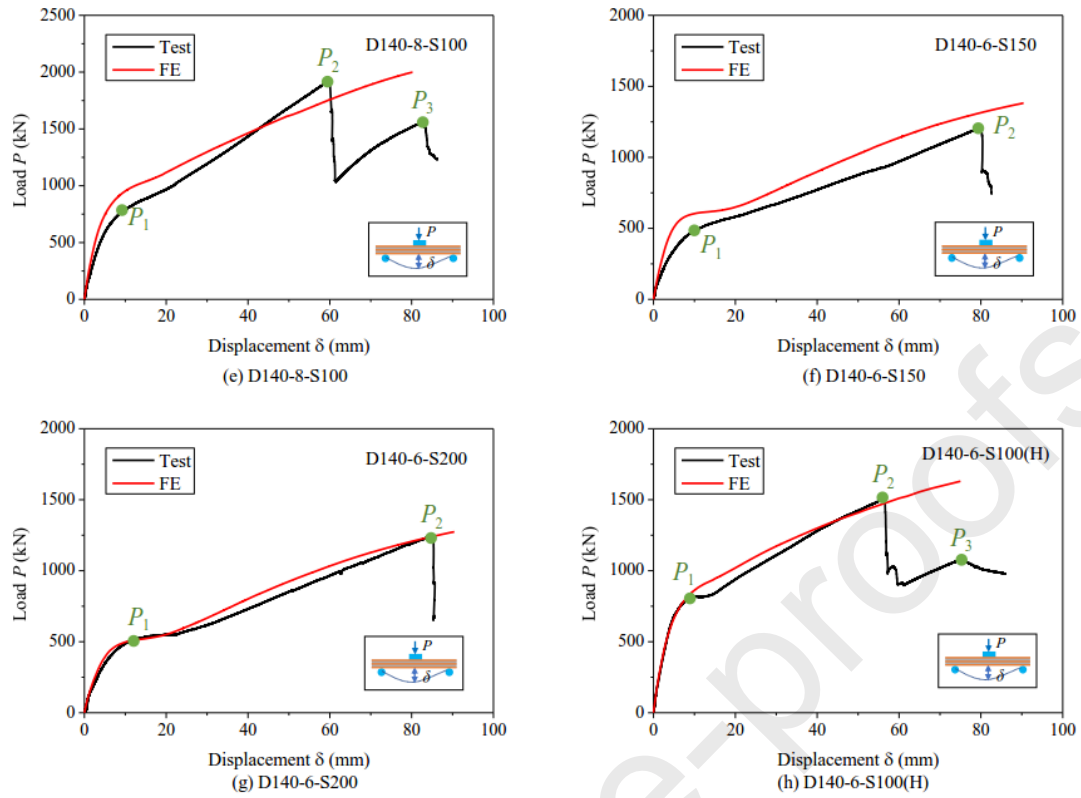
Draft, 1/22/2022

Figure 6 Comparison of load-displacement curves between test and FE

(e) D140-8-S100

(f) D140-6-S150

(g) D140-6-S200

(h) D140-6-S100(H)

Figure 6 Comparison of load-displacement curves between test and FE

(i) D140-6-S100(J)

(j) D140-6-S150(A150)

Figure 6 Comparison of load-displacement curves between test and FE

(a) D140-4-S100

(b) D140-6-S150
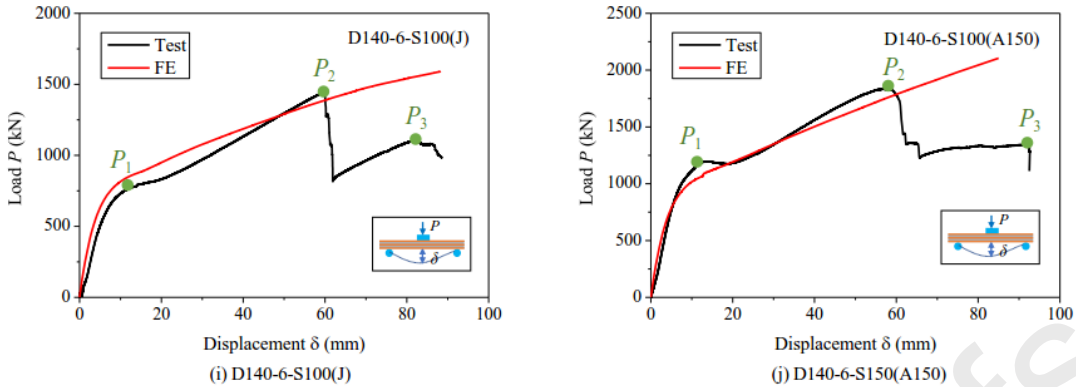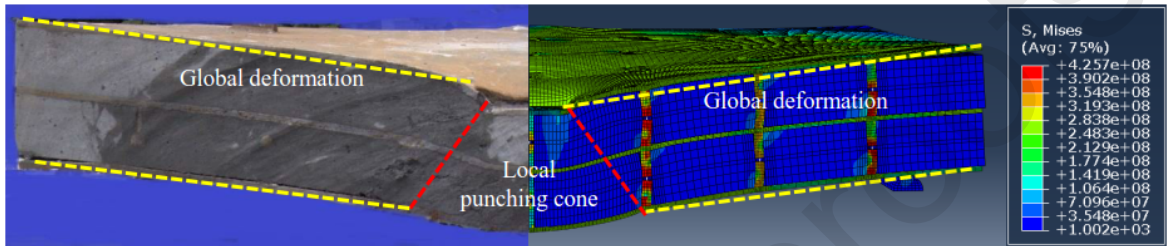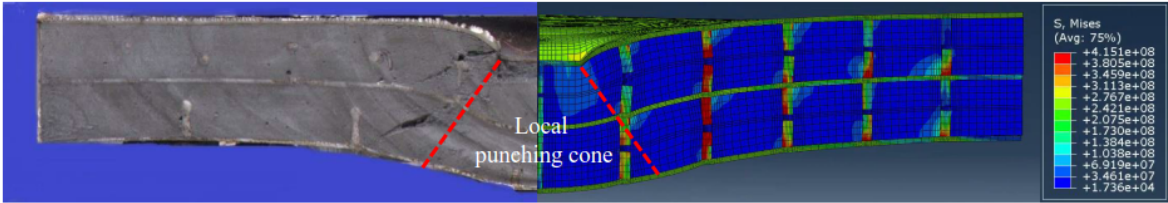
Figure 7 Comparison of failure modes between test and FE

(a) Load-displacement curve

(b) Stiffness
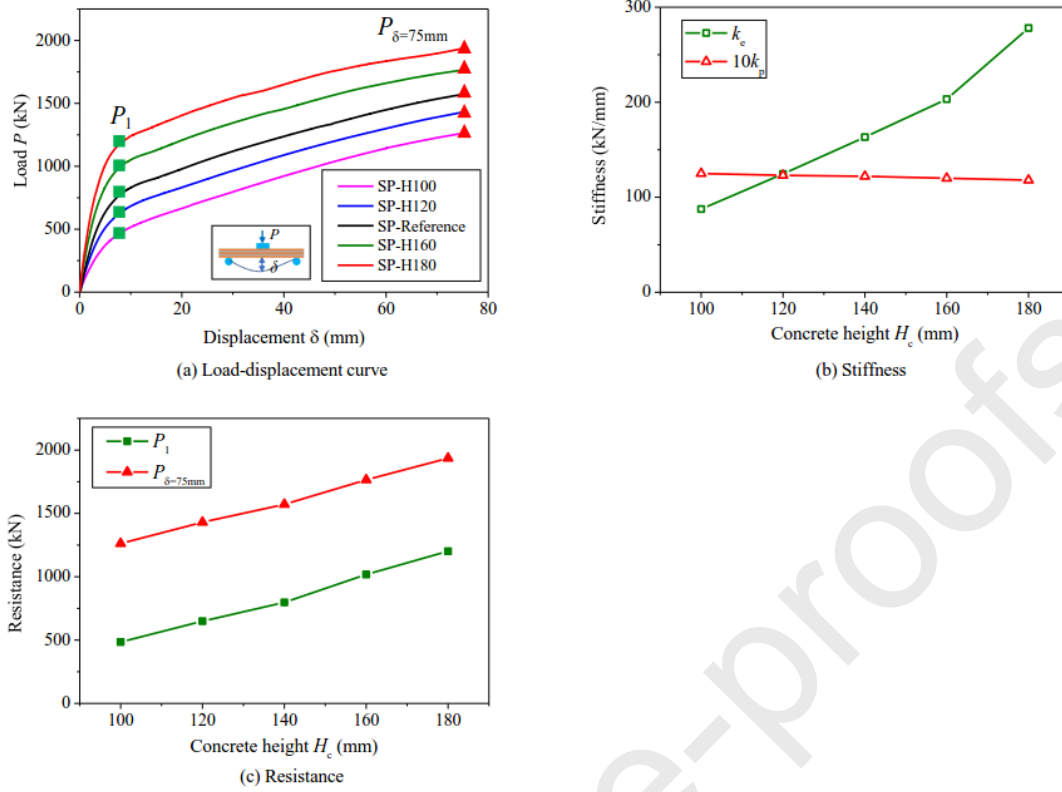
(c) Resistance

Figure 8 Effect of concrete height on stiffness and load resistance

(a) Load-displacement curve

(b) Stiffness
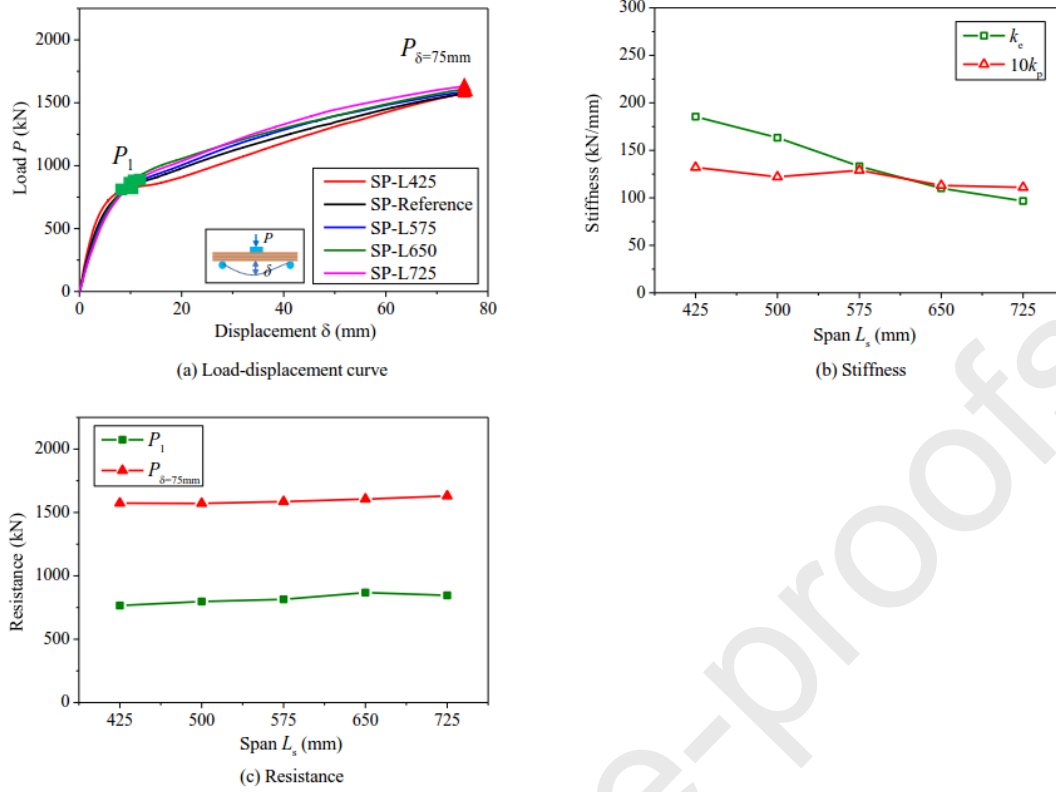
(c) Resistance

Figure 9 Effect of clear span on stiffness and load resistance

(a) Load-displacement curve

(b) Stiffness
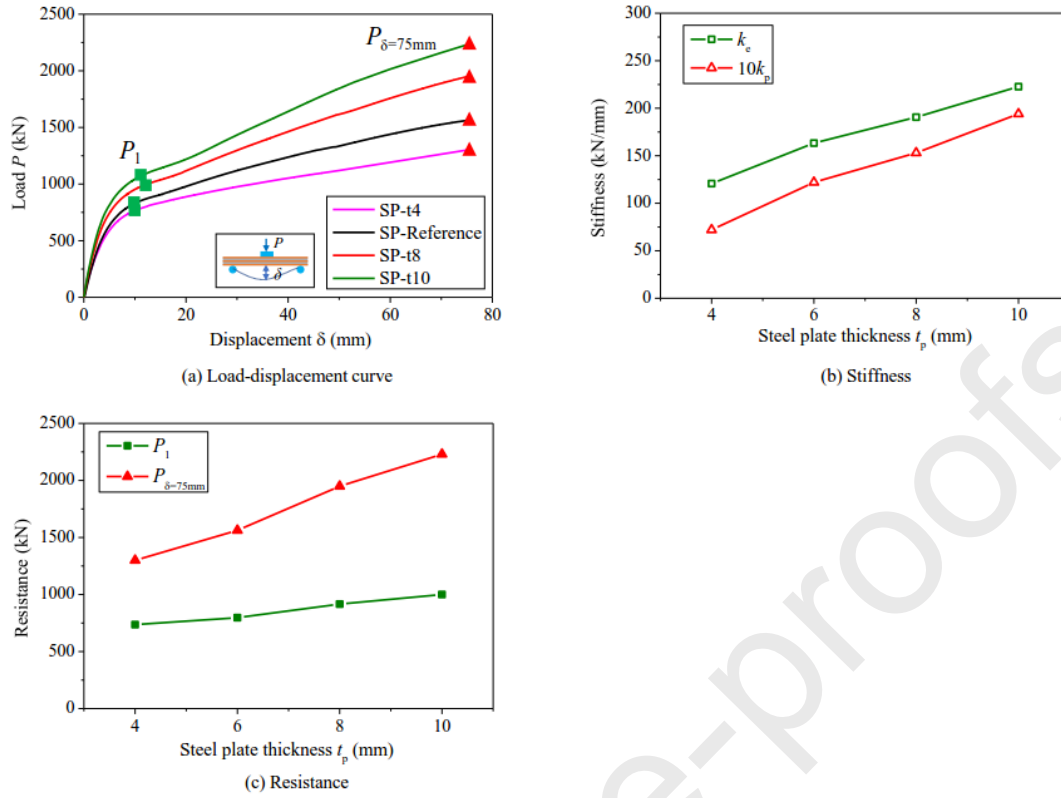
(c) Resistance

Figure 10 Effect of steel plate thickness on stiffness and load resistance

(a) Load-displacement curve

(b) Stiffness
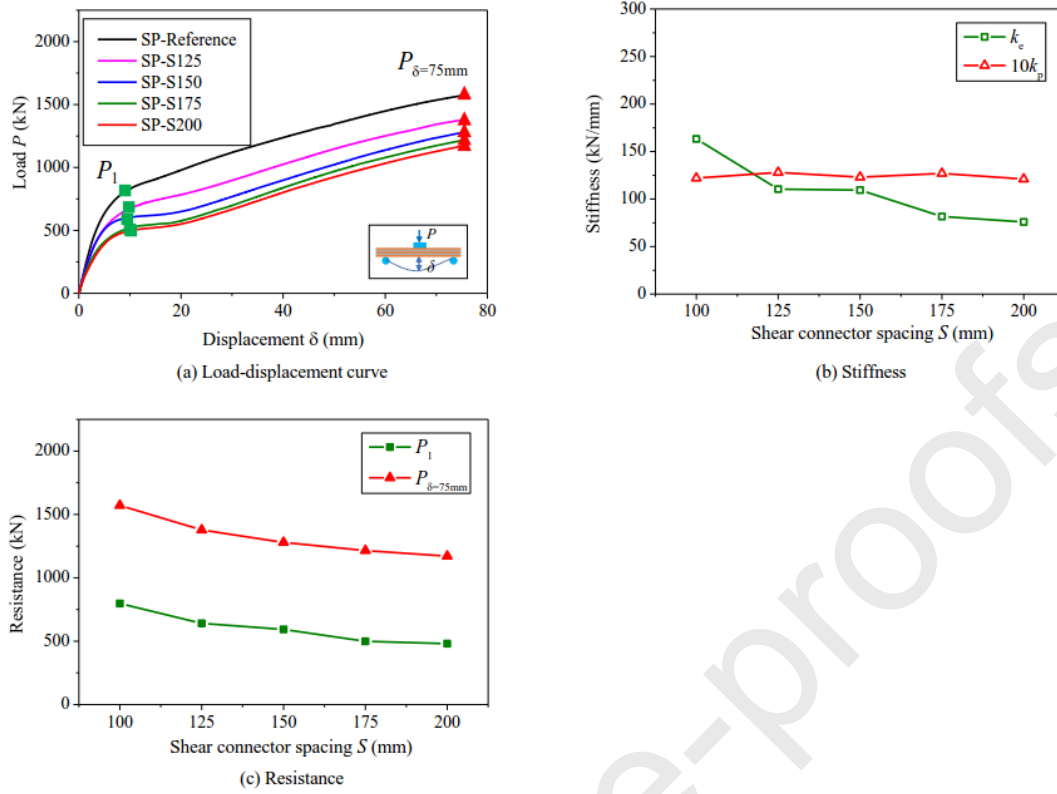
(c) Resistance

Figure 11 Effect of shear connector spacing on stiffness and load resistance

(a) Load-displacement curve

(b) Stiffness
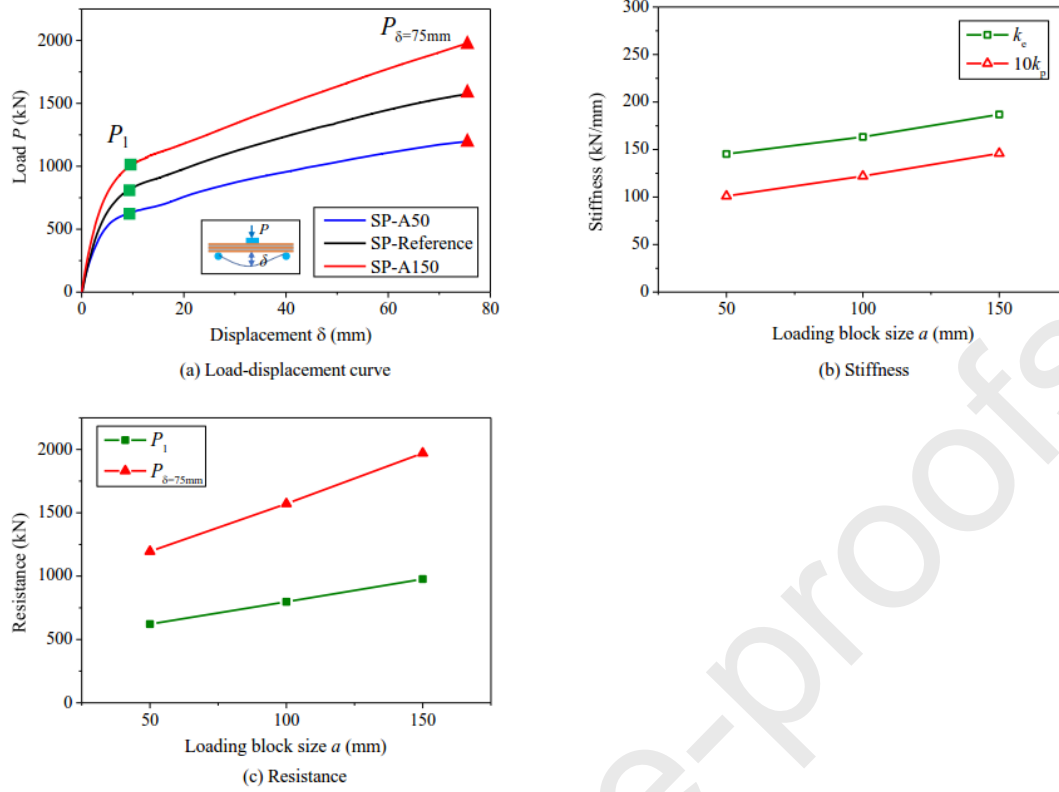
(c) Resistance

Figure 12 Effect of loading block size on stiffness and load resistance

(a) Load-displacement curve

(b) Stiffness
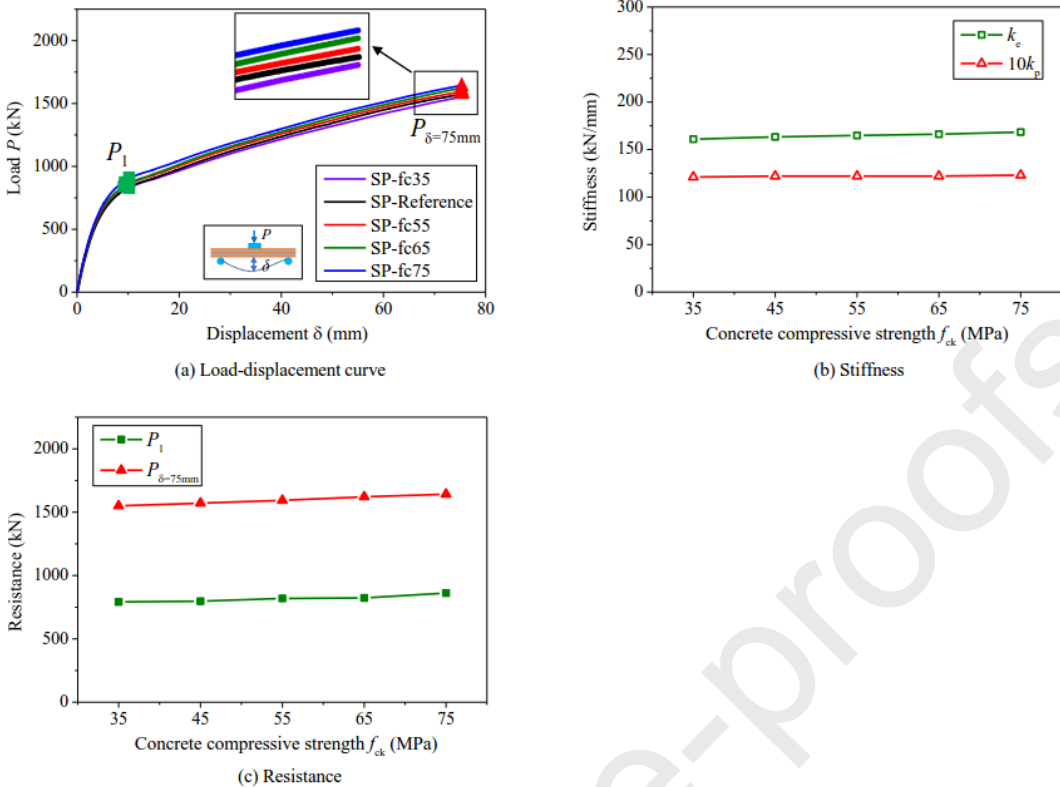
(c) Resistance

Figure 13 Effect of concrete compressive strength on stiffness and load resistance

(a) Load-displacement curve

(b) Stiffness
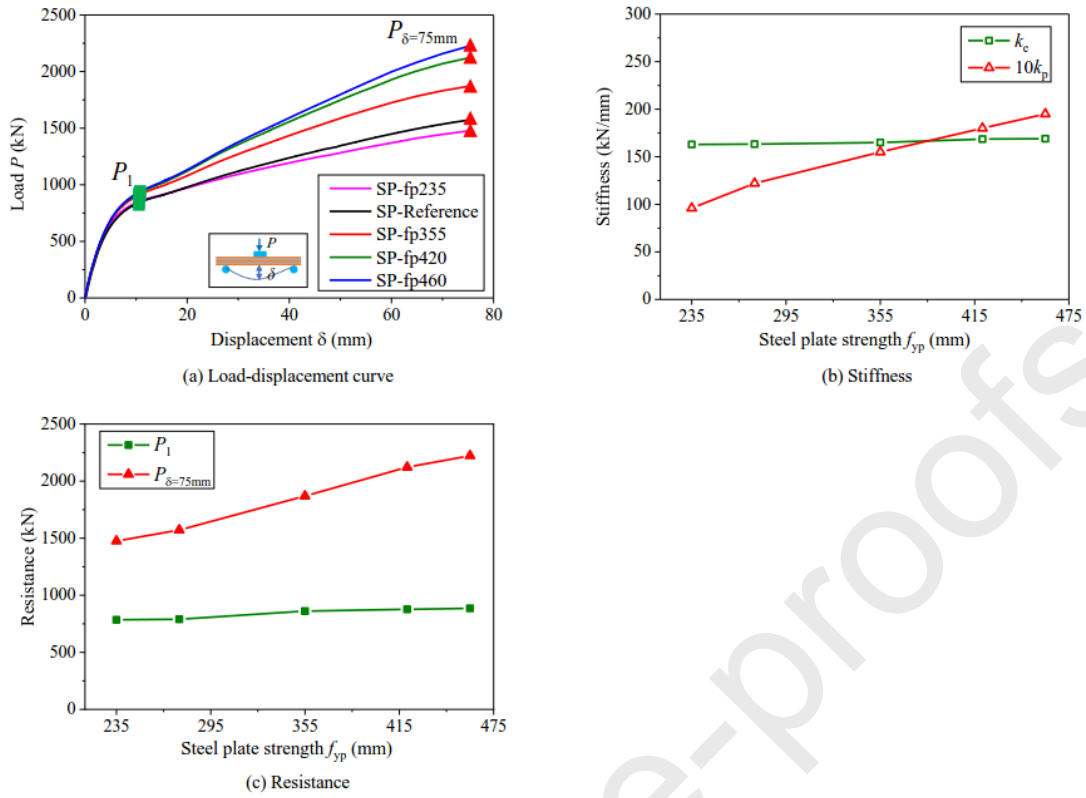
(c) Resistance

Figure 14 Effect of steel plate strength on stiffness and load resistance
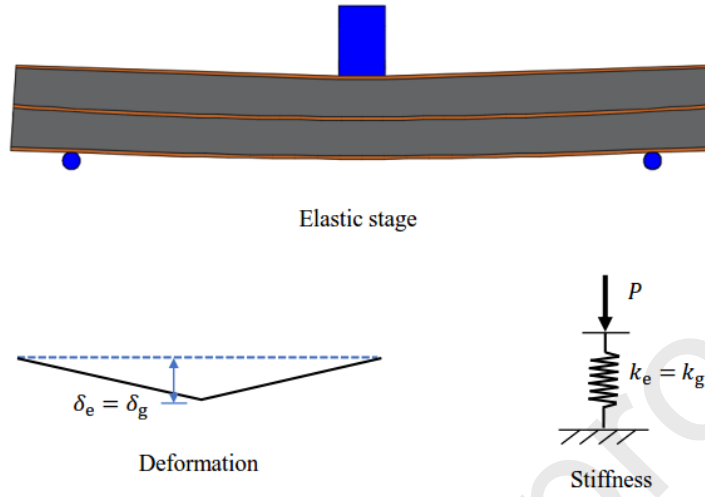
Figure 15 Deformation and stiffness of SCS panel at elastic stage

Draft, 1/22/2022
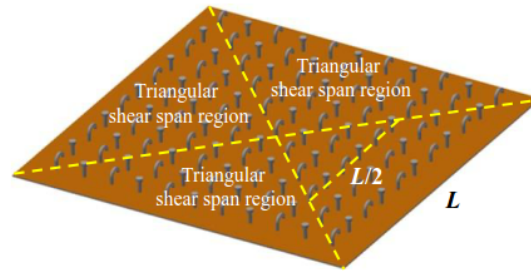
Figure 16 Illustration of triangular shear span
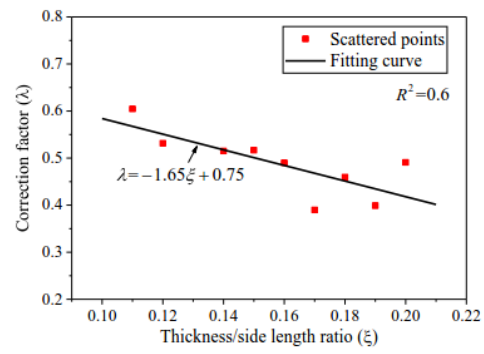
Figure 17 Correction factor in relation to the thickness/side length ratio
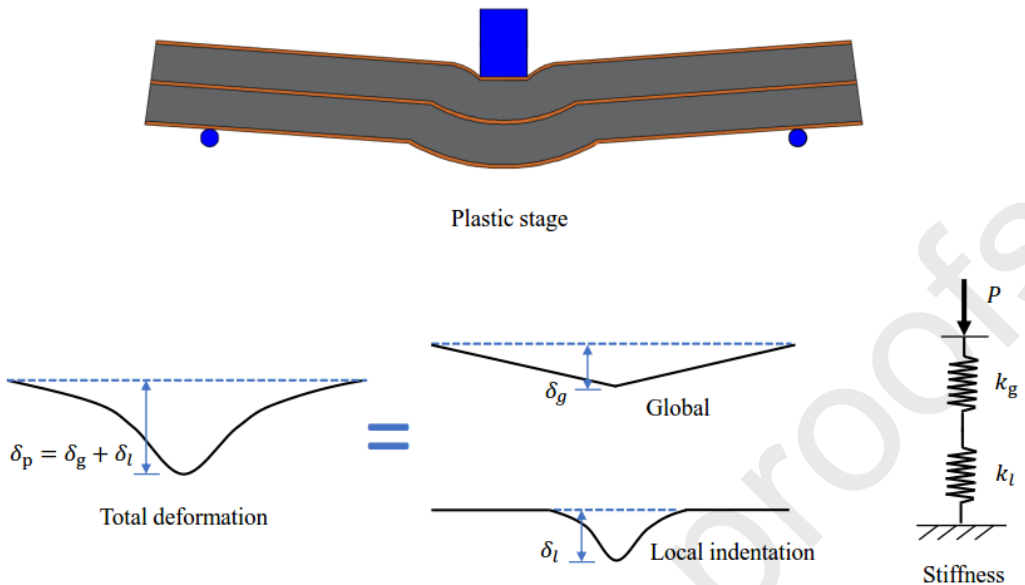
Figure 18 Deformation and stiffness of SCS panel at plastic stage
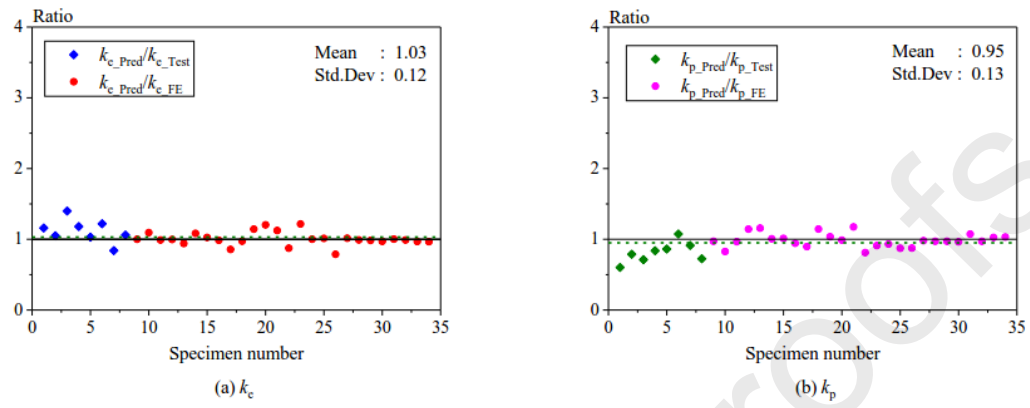
Figure 19 Prediction to Test (FE) ratio of k_c and k_p
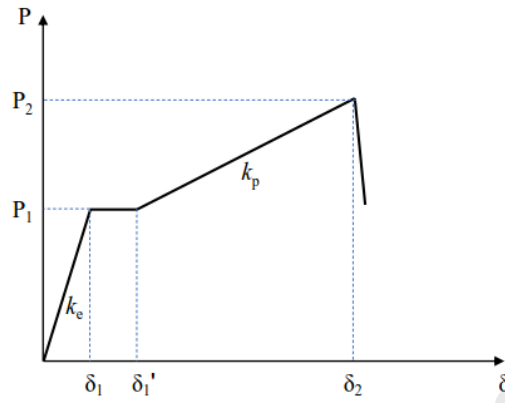
Figure 20 Idealized load-displacement curve
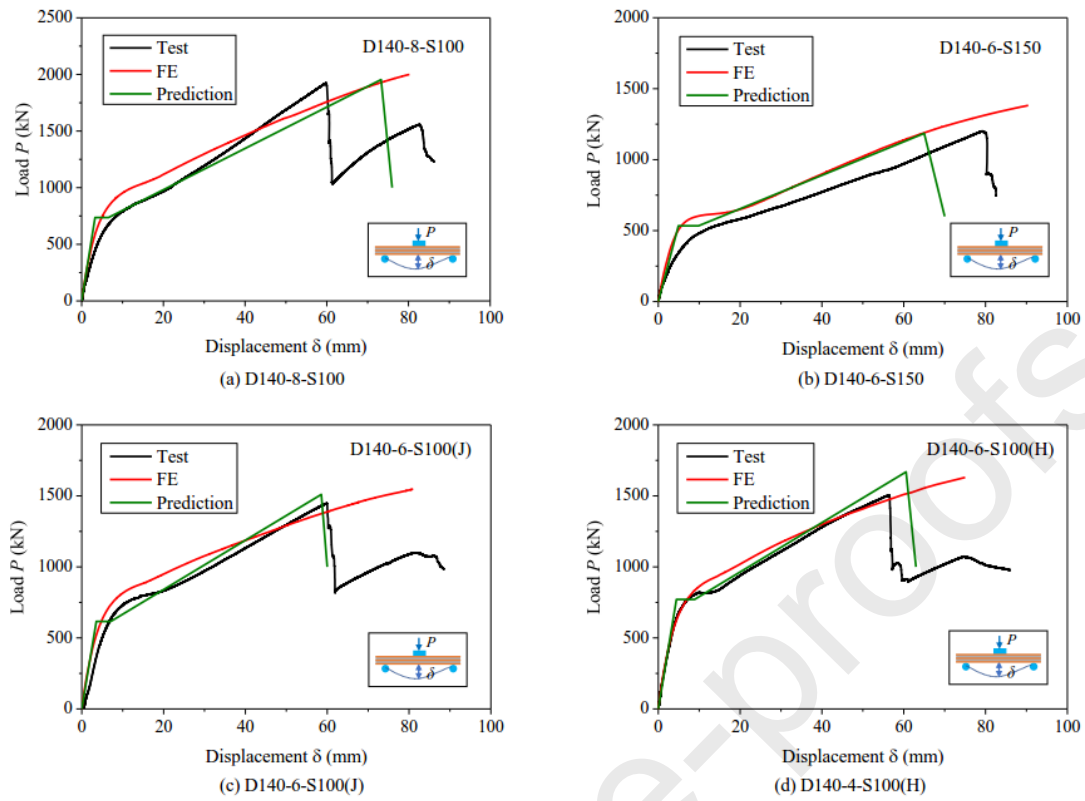
Figure 21 Comparison of load-displacement curves among test, FE and prediction

Declaration of interests

☒ The authors declare that they have no known competing financial interests or personal relationships that could have appeared to influence the work reported in this paper.

☐The authors declare the following financial interests/personal relationships which may be considered as potential competing interests:

Draft, 1/22/2022